Research Square

Preprints are preliminary reports that have not undergone peer review.
They should not be considered conclusive, used to inform clinical practice,
or referenced by the media as validated information.

A bio-inspired synthetic efferocytosis chimeric receptor restores macrophage efferocytosis and inflammatory resolution after cardiac injury

Zheyong Huang

zheyonghuang@126.com

Department of Cardiology, Zhongshan Hospital, Fudan University, Shanghai Institute of Cardiovascular Diseases

Xueyi Weng

Zhongshan Hospital, Fudan University

haipeng tan

the First Affiliated Hospital of Chongqing Medical University

Weiyan Li

Zhongshan Hospital, Fudan University

Zhiqing Pang

Fudan University https://orcid.org/0000-0003-0228-904X

Mengyuan Jiang

University of Science and Technology of China https://orcid.org/0009-0001-2430-0628

Shiteng Cai

Zhongshan Hospital, Fudan University

Danwen Zheng

Zhongshan Hospital, Fudan University

Jinfeng Gao

Fudan University

ailian lin

Westlake Genomics and Bioinformatics Lab

Sheng Zhao

Zhongshan Hospital, Fudan University

Yifei Yu

Fudan University

Jing Chen

Fudan University

qiaozi wang

Zhongshan hospital, Fudan University https://orcid.org/0000-0003-1820-2025

Qiyu Li
Zhongshan Hospital, Fudan University
Zhengmin Wang
Fudan University
Chengzhi Han
Zhongshan Hospital, Fudan University
Bohan Wei
Zhongshan Hospital, Fudan University
Yiwen Tan
Zhongshan Hospital, Fudan University
Yuyuan Fu
Zhongshan Hospital, Fudan University
Juying Qian
Zhongshan Hospital, Fudan University https://orcid.org/0000-0002-7512-3692
Yanan Song
Shanghai Institute of Cardiovascular Diseases, Zhongshan Hospital, Fudan University
Junbo Ge
Fudan University https://orcid.org/0000-0002-2549-0398

Article

Keywords:

Posted Date: February 25th, 2026

DOI: https://doi.org/10.21203/rs.3.rs-8532127/v1

License: This work is licensed under a Creative Commons Attribution 4.0 International License.
Read Full License

Additional Declarations: There is **NO** Competing Interest.

Abstract

Inflammation that fails to resolve after cardiac injury is a major driver of adverse tissue remodeling and heart failure. A central contributor to this failure is defective efferocytosis, in which macrophages incompletely clear apoptotic cells owing to disrupted coupling between apoptotic recognition and Mertk-dependent resolution signaling under inflammatory stress. Here we develop a bio-inspired efferocytic chimeric receptor (ECR) that restores efferocytosis by directly integrating phosphatidylserine recognition with intact Mertk intracellular signaling. By reconstructing this native clearance pathway at the receptor level, ECR enable macrophages to execute physiological efferocytosis when endogenous signaling is compromised. Using Ly6C antibody-modified lipid nanoparticles (LNP) to deliver ECR mRNA in vivo, we transiently program circulating monocytes and their derivative macrophages in the injured myocardium. In a mice model of cardiac ischemia-reperfusion (MI/R) injury, ECR expression enhanced macrophage efferocytosis, promoted resolution-associated signaling, and attenuates post-infarction inflammation, resulting in reduced tissue injury and improved cardiac function. Macrophages in ECR-treated hearts exhibit transcriptional features consistent with reparative and efferocytosis-linked states. A corresponding human ECR analog similarly enhanced efferocytosis and anti-inflammatory responses in human macrophages in vitro, supporting translational relevance. Together, these findings establish efferocytic receptor engineering combined with in situ mRNA delivery as a strategy to restore defective efferocytosis and enable resolution-focused immunomodulation after cardiac injury.

1. Introduction

Failure to resolve inflammation is a central determinant of adverse tissue remodeling following cardiac injury [1–3]. Myocardial infarction, particularly in the context of ischemia-reperfusion (MI/R), represents a paradigmatic clinical setting in which this failure of inflammatory resolution critically shapes long-term cardiac outcome [4]. Although timely reperfusion effectively limits acute cardiomyocyte death, post-ischemic inflammation often persists, promoting fibrosis and ventricular dysfunction [5, 6]. Increasing evidence indicates that maladaptive post-infarction inflammation is driven less by sustained immune overactivation than by insufficient execution of endogenous resolution programs required for tissue repair [7, 8].

Efferocytosis, the process by which macrophages recognize and clear apoptotic cells-plays a pivotal role in terminating inflammation and restoring tissue homeostasis [9]. Efficient engulfment of apoptotic cells not only removes cellular debris, but also reprograms macrophages toward anti-inflammatory and pro-resolving states [10]. When efferocytosis is compromised [11], apoptotic cells undergo secondary necrosis, releasing danger signals that prolong inflammation and disrupt tissue repair [12]. Accordingly, defective efferocytosis has emerged as a key pathological feature linking unresolved inflammation to maladaptive remodeling across multiple injury settings [13–15].

Recognition of apoptotic cells by macrophages is orchestrated by the phosphatidylserine (PS)-Growth arrest-specific 6 (Gas6)-Myeloid epithelial reproductive tyrosine kinase (Mertk) signaling axis [16]. In this pathway, PS exposed on apoptotic membranes is bridged to the Mertk receptor through ligands such as Gas6, triggering engulfment and downstream anti-inflammatory signaling [17]. Under conditions of acute inflammatory stress, however, this signaling axis is frequently disrupted by proteolytic Mertk cleavage, ligand insufficiency, and functional exhaustion of macrophages [18]. As a result, macrophages lose effective coupling between apoptotic recognition and efferocytic signaling, leading to persistent inflammatory activation [19].

Existing therapeutic strategies aimed at enhancing efferocytosis, including supplementation of soluble bridging molecules, pharmacological activation of Tyro3-Axl-MerTK (TAM) receptors, and administration of specialized pro-resolving mediators, have demonstrated efficacy in selected experimental settings [20–23]. However, these approaches primarily rely on extrinsic amplification of upstream signals and depend on intact receptor-ligand coupling and downstream signaling capacity within macrophages [21]. Under conditions of acute inflammation, such as myocardial infarction-reperfusion injury, this signaling architecture is often compromised, limiting the effectiveness of ligand-based or indirect interventions [24]. In parallel, recent work has explored chimeric phagocytic or efferocytic receptors that enhance apoptotic cell clearance by directly coupling target recognition to engulfment pathways [25, 26]. These studies establish the feasibility of receptor-level engineering to augment macrophage phagocytosis or efferocytosis. However, most existing designs are optimized to enforce engulfment itself, rather than to reconstitute the integrated signaling architecture that couples apoptotic cell recognition to Mertk-dependent resolution programs, which are selectively disrupted under inflammatory stress.

Building on this concept, we engineered a bio-inspired efferocytic chimeric receptor (ECR) designed to restore defective apoptotic cell clearance by reconstructing the PS-Gas6-Mertk axis in macrophages. This synthetic receptor integrates the PS-binding and receptor-activating modules of Gas6 with the native Mertk transmembrane and intracellular signaling domains. The Gas6-derived extracellular domains confer direct recognition of apoptotic cells, while the endogenous Mertk signaling domain ensures faithful propagation of efferocytic and anti-inflammatory programs. By synthetically reconstituting this physiological clearance pathway at the receptor level, ECR enable macrophages to sustain effective efferocytosis even under inflammatory conditions in which endogenous ligand availability or Mertk activation is compromised. To enable efficient in situ expression of this receptor, we employed an antibody-modified lipid nanoparticle (LNP)-based mRNA delivery strategy to transiently express the ECR in circulating monocytes and macrophages. This approach allows localized generation of ECR-expressing macrophages within injured cardiac tissue without ex vivo manipulation (Figure S1). Collectively, these findings establish bio-inspired efferocytic receptor engineering combined with in situ mRNA delivery as a strategy to restore defective efferocytosis and promote resolution-focused immunomodulation following tissue injury.

2. Result

2.1 Impaired efferocytosis and fibroblast activation in the infarct zone after MI

To investigate post myocardial infarction (MI) changes in macrophages and fibroblasts, we analyzed publicly available single-cell RNA-sequencing datasets from human myocardial tissue. The results revealed the enrichment of Mertk-positive cells within the monocyte/macrophage population (Fig. 1A). Compared with fibrotic regions, Mertk-positive macrophages are reduced in the infarct and border zones (Fig. 1B), and the phagocytic capacity of macrophages was markedly reduced in the infarcted area (Fig. 1C), accompanied by a pronounced activation of fibroblasts (Fig. 1D). These findings suggest that impaired clearance of necrotic cells by macrophages may contribute to sustained inflammation and subsequent fibrosis. Consistently, time-series analysis of murine data demonstrated a progressive decline in macrophage phagocytosis alongside increasing fibroblast activation over time (Fig. 1E-F). Together, these observations highlight a disruption of macrophage efferocytosis accompanied by fibroblast activation in the post-infarction myocardium. **2.2 Design and functional validation of efferocytic chimeric receptor (ECR)**

To reconstitute impaired efferocytosis under inflammatory conditions, we designed a bioinspired Efferocytic Chimeric Receptor (ECR) based on the endogenous phosphatidylserine (PS)-Gas6-Mertk signaling axis. During the phagocytosis process, macrophages utilize the bridging molecule Gas6 to recognize PS on apoptotic cells and activate Mertk-dependent phagocytic signaling. Gas6 contains two functional modules: a N-terminal γ-carboxyglutamic acid (Gla) domain responsible for PS recognition [27, 28] and a C-terminal laminin G-like (LG) domain required for receptor activation [29]. Accordingly, the ECR was constructed by fusing the PS-recognition and receptor-activating modules of Gas6 (Gla-LG) with the transmembrane and intracellular signaling domains of Mertk, separated by a CD8 hinge to ensure appropriate extracellular flexibility (Fig. 2A). Notably, the Mertk region incorporated into the ECR lacked the extracellular proteolytic cleavage site that is known to mediate Mertk shedding, thereby enhancing signaling stability under inflammatory conditions. This design enables direct sensing of PS on apoptotic cells while maintaining intact Mertk-dependent efferocytic signaling in acute myocardial infarction (Fig. 2A-B). Furthermore, two ECR variants: ECR(ΔGla), lacking the PS-binding module, and ECR(ΔMertk), lacking the intracellular signaling domain, were designed for subsequent functionality validation and mechanism exploration, and both variants exhibit essentially identical molecular weights to that of the ECR (Fig. 2A). Structural modeling and molecular dynamics simulations indicated that the engineered Gla-LG-Mertk receptor preserves the core Mertk fold while adopting a more open extracellular conformation, thereby facilitating flexible and stable interaction with PS-containing membranes (Figure S2, S3A). Upon ligand engagement, the receptor converged toward a more compact and energetically favorable state, consistent with productive receptor activation. These analyses support the rational design of ECR as a synthetic receptor capable of coupling PS recognition to Mertk signaling.

Then, we applied lipid nanoparticle (LNP) technology [30] to deliver mRNA encoding the ECR to macrophages and found that transient expression of the ECR could be achieved (Figure S3B-D). Flow

cytometric analysis of Flag and GFP reporters confirmed efficient receptor expression, with approximately 43.67 ± 0.90% of macrophages exhibiting detectable ECR expression (Figure S3E-F). Consistently, RT-qPCR and immunoblotting demonstrated robust ECR expression in bone marrow-derived macrophages (BMDMs), whereas control treatments showed minimal or undetectable signal (Fig. 2C, S3G). These data demonstrate that the engineered receptor can be effectively expressed in macrophages for downstream functional studies.

To evaluate ECR function, BMDMs transiently expressing ECR were co-cultured with fluorescently labeled apoptotic cardiomyocytes. Confocal microscopy demonstrated that macrophages expressing the complete ECR exhibited markedly enhanced engulfment of apoptotic cells compared with ECR(ΔGla) or ECR(ΔMertk) controls (Fig. 2D, S4A). Competitive blockade of PS recognition with Annexin V or inhibition of Mertk signaling substantially reduced engulfment, indicating that both the Gla-LG module and the Mertk intracellular domain are indispensable for receptor function (Fig. 2D, S4A). Flow cytometric quantification corroborated these findings (Fig. 2E, S4B), confirming that efferocytosis enhancement was strictly dependent on intact PS recognition and downstream Mertk signaling.

At the signaling level, we next examined the expression and γ-carboxylation of the Gas6-derived Gla-LG module (c-Gla), a post-translational modification required for Mertk activation [31]. To control for differences in receptor expression, c-Gla levels were normalized to the Flag tag. Robust c-Gla signals were readily detected in macrophages expressing the complete ECR, indicating efficient γ-carboxylation and functional availability of the Gla-LG module (Fig. 2F, S4C). In contrast, c-Gla signals were minimal or substantially reduced in variant receptor groups or under Annexin V and Mertk inhibition conditions (Fig. 2F, S4C). We then assessed activation of the intracellular signaling domain of the engineered receptor [32]. Immunoblot analysis revealed robust phosphorylation of Mertk (p-Mertk) in macrophages expressing the complete ECR, whereas p-Mertk levels were substantially reduced in the ECR(ΔGla) and Annexin-treated groups, and nearly undetectable in the ECR(ΔMertk) and Mertk inhibition groups (Fig. 2G, S4D). Consistent with effective efferocytic signaling [33], activation of the downstream effector Rac1 was most pronounced in ECR-expressing macrophages, whereas minimal activation was observed in variant receptor groups or in conditions where PS recognition or Mertk signaling was inhibited (Fig. 2H and Figure S4E).

Furthermore, RT-qPCR analysis demonstrated that expression of the complete ECR significantly enhanced activation of Mertk associated downstream pathways, including PI3K-AKT and MAPK/ERK signaling [34], whereas these responses were blunted in variant or inhibitor-treated groups (Fig. 2I). Collectively, these results demonstrate that the engineered ECR functions as an efferocytic receptor capable of coupling PS recognition to Mertk mediated signaling, supporting the re-establishment of coordinated efferocytic responses in macrophages

2.3 Design and characterization of a Ly6c-targeting lipid nanoparticle (LNP)

To enable in situ expression of the engineered ECR in monocytes and macrophages within infarcted myocardium, we developed Ly6c antibody-modified lipid nanoparticles (aLNP) as a delivery vehicle for ECR-encoding mRNA (aLNP-ECR). Given the robust recruitment of Ly6c high inflammatory monocytes to the injured heart following myocardial infarction, Ly6c was selected as a targeting moiety to facilitate selective mRNA delivery to this cell population. Lipid nanoparticles were formulated using the clinically validated SM-102 lipid system [35], and Ly6c antibodies were subsequently conjugated to the nanoparticle surface through chemical modification without perturbing particle assembly (Fig. 3A). Transmission electron microscopy (TEM) showed that both LNP-ECR and aLNP-ECR (aLNP) were uniform, spherical particles with regular morphology (Fig. 3B). Antibody conjugation resulted in minor increases in particle size and surface charge, whereas particle uniformity, colloidal stability, and mRNA encapsulation efficiency were maintained (Figure S5A-G). Nano-flow cytometry confirmed efficient surface display of Ly6c antibodies on aLNP (Fig. 3C, S5H), and encapsulated mRNA remained protected from serum degradation (Figure S5I).

We next evaluated the targeting capability of aLNP toward inflammatory Bone Marrow Mononuclear Cells (BMMNCs) in vitro. Compared with non-targeted LNP, aLNP exhibited significantly enhanced association with inflamed BMMNCs, as shown by confocal imaging and flow cytometry (Fig. 3D, S5J-K). This enhanced association was markedly attenuated by Ly6c blocking, confirming consistent with Ly6c-dependent (Fig. 3D, S5J-K). Following uptake, intracellular trafficking analysis demonstrated progressive dissociation of aLNP delivered mRNA from lysosomal compartments over time, indicating efficient endosomal escape and cytoplasmic delivery of the mRNA cargo (Fig. 3E).

The in vivo biodistribution of aLNP was subsequently examined in a mouse myocardial ischemia-reperfusion (MI/R) model. In vivo imaging revealed preferential accumulation of aLNP within infarcted cardiac tissue compared with non-targeted LNP

(Fig. 4F), while both formulations exhibited comparable distribution in other major organs (Figure S6A). Flow cytometric analysis further demonstrated enhanced association of aLNP with circulating Ly6c$^+$ monocytes and increased delivery to F4/80$^+$ macrophages in the injured myocardium, supporting monocyte-mediated transport of aLNP to the infarcted heart (Figure S6B-E). Immunofluorescence staining further confirmed preferential localization of DiD labeled aLNP within the peri-infarct region, where they showed more pronounced colocalization with CD11b$^+$ cells compared with non-targeted LNP (Fig. 3G, S6F-I). Collectively, these findings indicate that aLNP is delivered to sites of cardiac injury via monocyte-mediated trafficking.

To confirm functional mRNA delivery in vivo, GFP encoded within the ECR construct was used as a reporter. Mice treated with aLNP exhibited higher proportions of GFP$^+$ Ly6c$^+$ monocytes in peripheral blood and GFP$^+$ F4/80$^+$ macrophages in infarcted cardiac tissue compared with non-targeted LNP (Fig. 3H-I, S7A-D). Together, these results establish Ly6c-targeting LNP as an effective delivery platform that enables localized expression of ECR in monocyte-macrophage lineages, thereby supporting in vivo macrophage engineering within injured myocardium.

2.4 Functional evaluation of ECR-expressing macrophages in vitro

The primary objective of this study was to enhance macrophage phagocytosis through the construction of engineered ECR. As described above, LNP-mediated mRNA delivery enabled transient expression of ECR in macrophages (ECR-M). We next investigated whether ECR expression functionally augmented macrophage efferocytosis and reshaped their inflammatory phenotype (Fig. 4A). To control for potential effects of Ly6c antibody modification, an aLNP formulation carrying non-coding mRNA (aLNP-mRNA) was included. Apoptotic HL-1 cardiomyocytes were co-incubated with inflammatory BMDMs previously treated with LNP-mRNA, aLNP-mRNA, LNP-ECR, or aLNP-ECR. Immunofluorescence analysis showed substantially greater engulfment of apoptotic cells by ECR-expressing macrophages (Fig. 4B). Quantitatively, efferocytosis rates reached 35.0% ± 5.0% in the LNP-ECR group and 75.0% ± 5.0% in the aLNP-ECR group, compared with 5.0% ± 5.0% and 6.7% ± 2.9% in the LNP-mRNA and aLNP-mRNA controls, respectively (Fig. 4C). This enhancement was further confirmed by flow cytometry (Figure S8A-B), indicating that ECR expression markedly increases macrophage efferocytotic capacity.

Given the established relationship, between efferocytosis and macrophage functional state, we next examined whether ECR-mediated phagocytosis induces transcriptional reprogramming. Bulk RNA sequencing revealed that ECR-expressing macrophages occupied a distinct transcriptional space, as demonstrated by unbiased principal component analysis (Fig. 4D). Differential gene expression analysis showed downregulation of pro-inflammatory, M1-associated genes and concurrent upregulation of M2-associated and reparative genes in the aLNP-ECR group (Fig. 4E-F). Consistently, pathway enrichment analysis identified activation of phagosome formation, cytokine-cytokine receptor interaction, and PI3K-AKT signaling, alongside attenuation of inflammatory pathways including NF-κB and IL-17 signaling (Fig. 4G). These transcriptional patterns are consistent with a shift toward an inflammation-resolving phenotype following ECR expression and enhanced efferocytosis. Phenotypic analyses corroborated these findings. Immunofluorescence staining demonstrated a reduction in $iNOS^+$ M1-like macrophages and a parallel enrichment of $CD206^+$ M2-like macrophages after LNP-ECR or aLNP-ECR treatment, with the most pronounced effect observed in the aLNP-ECR group (Fig. 4H, S8C). Flow cytometric analysis confirmed these changes (Fig. 4I, S9). Moreover, RT-qPCR analysis confirmed significant downregulation of M1 markers (iNOS, IL-1β, and IL-6) and upregulation of M2 markers (Arg1, IL-10, and YM-1) in macrophages treated with aLNP-ECR (Figure S8D-E). Collectively, these findings demonstrate that ECR expression not only enhances macrophage efferocytosis but also actively reprograms macrophages toward an anti-inflammatory, tissue-reparative phenotype.

2.5 aLNP-ECR promotes infarct repair and functional recovery after MI/R

To evaluate the therapeutic efficacy of aLNP-ECR in vivo, a mouse myocardial ischemia-reperfusion (MI/R) model was established, and cardiac function and structural remodeling were assessed (Fig. 5A). Compared with control groups, mice treated with aLNP-ECR exhibited a significantly reduced infarct size,

as determined by TTC staining (Fig. 5B). Longitudinal echocardiographic analysis revealed that aLNP-ECR treated mice showed sustained preservation of left ventricular ejection fraction (LVEF) and fractional shortening over time, together with attenuation of post-infarction ventricular dilation, as reflected by reduced increases in left ventricular end-diastolic (LVEDV) and end-systolic volumes (LVESV) (Fig. 5C). Histological evaluation at 28 days after MI/R further supported these findings. Hearts from aLNP-ECR treated mice displayed increased residual left ventricular wall thickness and reduced fibrotic scar formation, as assessed by hematoxylin and eosin and Masson's trichrome staining (Fig. 5D-E). Quantitative analyses confirmed a significant reduction in scar area and preservation of ventricular wall thickness in the aLNP-ECR group compared with control treatments (Fig. 5E). Together, these data indicate that aLNP-ECR treatment is associated with reduced infarct size, improved cardiac function, and attenuation of adverse ventricular remodeling following MI/R.

2.6 aLNP-ECR enhances macrophage efferocytosis and reshapes the post-infarction immune microenvironment in vivo

Given that aLNP-ECR is designed to enhance macrophage efferocytosis, we next examined phagocytic activity within the injured myocardium. Using α-MHCCre: Rosa26-tdTomato mice, in which cardiomyocytes are specifically labeled, we observed a significant increase in the proportion of tdTomato$^+$ macrophages following aLNP-ECR treatment, indicating enhanced cardiomyocyte efferocytosis in vivo (Fig. 6A, S10A). Spatial analysis by confocal imaging revealed that tdTomato signals within macrophages were predominantly detected in the infarct border zone, whereas tdTomato-positive macrophages were rarely observed in remote regions (Fig. 6B, S10B). This spatial restriction indicates that ECR-enhanced efferocytosis is confined to areas of injury and does not promote aberrant phagocytosis of viable cardiomyocytes in non-ischemic myocardium. Consistent with enhanced efferocytic clearance, the number of residual Tunel$^+$ apoptotic cells within the border zone was significantly reduced in aLNP-ECR treated hearts (Fig. 6C). These results indicate that aLNP-ECR enhances efferocytosis primarily within injured myocardium without evidence of widespread engulfment in non-ischemic tissue.

We next examined whether increased efferocytosis was associated with alterations in the post-infarction immune microenvironment. Flow cytometric analysis revealed a pronounced shift in macrophage phenotype, characterized by a reduction of CD86$^+$ pro-inflammatory macrophages and an expansion of CD206$^+$ reparative macrophages following aLNP-ECR treatment (Fig. 6D, S11). Mechanistically, this phenotypic transition was accompanied by increased phosphorylation of Mertk and activation of downstream PI3K-AKT-ERK signaling pathways (Fig. 6E-F). In parallel, cardiac levels of pro-inflammatory cytokines were reduced (Fig. 6G), whereas anti-inflammatory mediators and specialized pro-resolving lipid mediators were significantly elevated (Fig. 6G, S12A). Bulk RNA sequencing of infarct regions further revealed coordinated upregulation of genes associated with efferocytosis, anti-inflammatory signaling, and macrophage reparative programs, alongside suppression of inflammatory pathways in aLNP-ECR treated hearts (FigureS12B-C). Collectively, these data show that aLNP-ECR enhances

cardiomyocyte efferocytosis in vivo and is associated with coordinated remodeling of the post-infarction immune microenvironment toward a resolution-oriented state.

2.7 Single-cell transcriptomic profiling of lesional macrophages after aLNP-ECR treatment

To define how aLNP-ECR reshapes the immune landscape within the infarcted myocardium, particularly the heterogeneity and functional states of lesional macrophages, we performed single-cell RNA sequencing (scRNA-seq) on leukocytes isolated from infarct regions of MI/R hearts treated with PBS or aLNP-ECR. Unsupervised clustering and UMAP visualization identified four major immune cell populations: macrophages/monocytes, granulocytes, B cells and T/NK cells-based on canonical marker genes (Fig. 7A). Macrophages constituted the dominant leukocyte population in both groups. At the global immune level, relative proportions of macrophages and granulocytes showed modest shifts following aLNP-ECR treatment, while other immune populations remained largely unchanged (Figure S13A). Given the central role of macrophages in efferocytosis and post-infarction repair, we next focused on the macrophage compartment. Reclustering analysis revealed seven transcriptionally distinct macrophage states, including Spp1^{+} reparative, inflammatory, metabolic-active, MHC-II^{+} antigen-presenting, proliferating, interferon-responsive and resident reparative subsets (Fig. 7B). aLNP-ECR treatment was associated with a redistribution of these subsets, characterized by relatively higher proportions of reparative and metabolically active clusters and a lower contribution from inflammatory macrophages (Figure S13B). These compositional changes are consistent with macrophage state redistribution toward reparative programs within the infarct niche, rather than direct inference of lineage conversion.

To directly assess whether these compositional shifts were accompanied by functional reinforcement of efferocytosis-related programs, we next examined functional gene signatures across macrophage subsets. Macrophages from aLNP-ECR treated hearts exhibited significantly higher efferocytosis scores across multiple subsets compared with PBS controls (Fig. 7C). Concordantly, MacSpectrum analysis showed increased phagosome-lysosome gene signature scores in the aLNP-ECR group (Fig. 7D), indicating transcriptional enhancement of efferocytic programs. In parallel, macrophages from aLNP-ECR hearts exhibited lower expression of pro-inflammatory gene signatures and higher expression of anti-inflammatory programs across multiple subsets (Fig. 7E), consistent with the cytokine profiles and bulk RNA-seq obtained from infarct tissue.

We next investigated whether aLNP-ECR influences the dynamic progression of lesional macrophages by performing trajectory and pseudotime analyses. When projected onto the inferred macrophage trajectory, cells from PBS treated hearts predominantly occupied early pseudotime regions associated with inflammatory and IFN-responsive states, whereas macrophages from aLNP-ECR treated hearts were redistributed toward later pseudotime positions enriched for metabolically active and reparative states (Fig. 7F). Pseudotime-resolved analysis further revealed a progressive increase in efferocytosis and phagosome-lysosome gene programs along the macrophage trajectory (Fig. 7G,7H). Notably,

aLNP-ECR treated macrophages displayed higher efferocytosis-related scores across the trajectory, with earlier and more pronounced induction of these programs at comparable pseudotime positions relative to PBS controls, suggesting that aLNP-ECR accelerates the acquisition and strengthening of efferocytic capacity along the macrophage continuum. Consistent with these findings, pathway enrichment analysis of differentially expressed genes further indicated that genes upregulated in lesional macrophages after aLNP-ECR treatment were enriched in endocytosis, phagosome formation, and MAPK signaling pathways, whereas genes downregulated were predominantly associated with chemokine signaling and inflammatory pathways including TNF and IL-17 signaling, as well as apoptosis-related processes (Fig. 7I). Finally, cell-cell communication analysis suggested enhanced outgoing signaling from macrophage subsets toward cardiac fibroblasts in aLNP-ECR treated hearts (Fig. 7J), raising the possibility that ECR-programmed macrophages may influence fibroblast behavior during post-infarction remodeling. Collectively, these single-cell analyses indicate that aLNP-ECR treatment is associated with reinforcement of efferocytosis-linked, reparative transcriptional programs across multiple lesional macrophage states, providing transcriptomic support for the in vivo functional and immunological remodeling observed in earlier analyses.

2.8 Safety Evaluation of aLNP-ECR

The cytotoxicity and in vivo biosafety of aLNP-ECR were systematically evaluated. In vitro CCK-8 assays showed no detectable cytotoxicity of aLNP-ECR toward BMDMs (Figure S14A). To assess systemic safety, healthy mice were intravenously administered PBS or aLNP-ECR, followed by comprehensive immunological and organ function analyses. Serum levels of pro-inflammatory cytokines (TNF-α and IL-1β) measured three days after administration were comparable between groups (Figure S14B). Likewise, circulating immunoglobulin G (IgG) and immunoglobulin M (IgM) levels showed no significant differences, indicating absence of overt humoral immune activation (Figure S14C). Evaluation of coagulation parameters (activated partial thromboplastin time (APTT), prothrombin time (PT), fibrinogen (Fbg)) and hepatic and renal function markers (alanine aminotransferase (ALT), aspartate aminotransferase (AST), creatinine (CREA), and blood urea nitrogen (UREA)) revealed no abnormalities in aLNP-ECR treated mice relative to controls (Figure S14D-F). Histological examination further confirmed the absence of discernible pathological changes in major organs (Figure S14G). Collectively, these data indicate that aLNP-ECR displays a favorable safety and tolerability profile under the conditions tested, supporting its further investigation in therapeutic settings.

2.9 Generation and characterization of human ECR

To assess the translational potential of the efferocytic chimeric receptor strategy, we constructed a human ECR comprising the human Gas6-derived Gla-LG module as the extracellular recognition domain and the transmembrane and intracellular domains of human Mertk (Fig. 8A). Delivery of ECR-encoding mRNA via LNP enabled efficient ECR expression in human macrophages, as confirmed by flow cytometric detection of the Flag tag (Fig. 8B). We then assessed whether ECR expression functionally modulates efferocytic activity in human macrophages. Compared with LNP and non-functional mRNA controls, ECR-expressing macrophages exhibited a significantly increased uptake of apoptotic

cardiomyocytes, as determined by flow cytometry (Fig. 8C-D), indicating enhanced efferocytic capacity. Consistent with this functional change, ECR-expressing human macrophages displayed a phenotypic shift characterized by increased expression of the M2-associated marker CD206 and reduced expression of the M1-associated marker CD86 (Fig. 8E-F). Moreover, cytokine analysis of culture supernatants revealed elevated production of the anti-inflammatory mediators TGF-β and IL-10, accompanied by reduced secretion of the pro-inflammatory cytokines TNF-α and IL-1β (Fig. 8G). Collectively, these results demonstrate that human ECR expression is sufficient to enhance macrophage efferocytosis and promote an anti-inflammatory phenotype in vitro, supporting the translational feasibility of the ECR strategy in human macrophages.

3. Discussion

Defective efferocytosis is increasingly recognized as a key barrier to inflammation resolution after myocardial infarction-reperfusion injury [9]. Although macrophages possess an intrinsic capacity to recognize and clear apoptotic cardiomyocytes, this program frequently becomes uncoupled from downstream resolution signaling in the inflamed post-infarction environment, leading to persistent inflammation and adverse remodeling [36]. In this study, we addressed this failure by restoring efferocytic function through receptor-level reconstitution that physiologically couples apoptotic cell recognition to resolution-associated macrophage programs. We engineered an efferocytic chimeric receptor (ECR) that directly links PS recognition to intact Mertk intracellular signaling. By integrating a Gas6-derived PS-binding module with the endogenous Mertk transmembrane and intracellular domains, ECR preserved native efferocytosis signaling while bypassing extracellular constraints that impair Mertk activation in inflamed tissue. Transient in situ expression of ECR via Ly6C-targeted mRNA-LNP selectively enhanced apoptotic cell clearance within injured myocardium, promoted resolution-associated macrophage programs, and improved post-infarction repair without inducing aberrant phagocytosis or systemic immune activation. Consistent with these functional effects, single-cell transcriptomic analysis revealed a redistribution of lesional macrophages toward reparative and metabolically active states, accompanied by coordinated enhancement of efferocytosis-related gene programs and attenuation of inflammatory signaling. These findings indicate that restoration of integrated efferocytosis signaling at the receptor level is sufficient to re-engage endogenous efferocytosis programs in inflamed tissue. Rather than relying on amplification of upstream ligands or diffusible mediators, ECR-based reprogramming reinstates the functional linkage between apoptotic cell sensing and Mertk-dependent signaling, enabling effective efferocytosis even when endogenous pathway activity is compromised.

This approach differs conceptually from engineered immune cell strategies in cardiovascular disease that focus on depletion of stable cellular populations, such as fibroblast activation protein-directed CAR T or CAR macrophage therapies developed for established fibrotic remodeling [37, 38]. In contrast, ECR couple macrophage efferocytic activation directly to the presence of apoptotic cells by recognizing phosphatidylserine as a universal “eat-me” signal and engaging downstream efferocytosis signaling [39]. As a result, receptor activation preferentially occurs under conditions of increased apoptotic burden,

aligning macrophage activity with endogenous inflammation resolution rather than sustained cell elimination. Myocardial infarction-reperfusion injury offers a clinically relevant example in which defective efferocytosis during the acute inflammatory phase contributes to adverse tissue remodeling [40]. More broadly, impaired efferocytosis is a shared feature of multiple inflammatory and degenerative conditions [41–43], suggesting that receptor-based reconstruction of resolution pathways may have applications beyond the cardiovascular system.

Several limitations merit consideration. The present study focuses on acute myocardial ischemia-reperfusion injury, and further work will be required to define optimal timing, durability, and disease specificity of ECR-based reprogramming in other pathological contexts. In addition, although transient mRNA-LNP delivery limits prolonged receptor expression [44], systematic evaluation of repeated dosing, dose-response relationships, and inter-individual immune variability will be essential for clinical translation.

In summary, this study establishes efferocytic receptor engineering as a strategy for functional reprogramming of macrophages in injured tissue. By restoring signaling competence within an endogenous apoptotic cell–clearance pathway, ECR-based immunomodulation promotes inflammation resolution and tissue repair, with potential relevance to inflammatory diseases characterized by defective efferocytosis.

4. Method

4.1 ECR Construction and mRNA Synthesis

We first employed molecular dynamics simulations using Gromacs to investigate the differences between native GAS6, Mertk and our designed ECR in terms of their affinities for the cell membrane and the stability of their protein structures. The molecular dynamics simulation systems were subjected to energy minimization using the steepest descent algorithm. Both isothermal-isochoric (NVT) and isothermal-isobaric (NPT) ensemble equilibrations were performed for 100,000 steps each, with a coupling constant of 0.1 ps and a total duration of 100 ps. Production molecular dynamics simulations were carried out for 5,000,000 steps with a time step of 2 fs, corresponding to a total simulation time of 100 ns. After completion of the simulations, the trajectories were analyzed using the built-in tools of the software to calculate the solvent-accessible surface area, distance variations, root mean square deviation, energy changes, free energy landscapes, root mean square deviation, root mean square fluctuation and secondary structure changes from the simulation trajectories. The ECR we designed consists of a murine-specific Gas6-derived Gla-LG, a CD8 hinge region, and a murine Mertk transmembrane domain together with intracellular co-stimulatory and signaling domains. Human ECR construct comprises a human Gas6-derived Gla-LG, a human CD8 hinge, and the transmembrane and intracellular signaling domains of human Mertk. A Flag tag and GFP were fused to the construct, respectively, to facilitate evaluation of gene transfer efficiency and assessment of in situ macrophage programming. All mRNA sequences are in Supplementary Table 1 and Supplementary Table 2. The

mRNA sequence encoding ECR was obtained from the UniProt database. The mRNA encoding this construct was custom-synthesized by Shanghai CYNBIO Biotechnology Co., Ltd.

4.2 Synthesis and Characterization of the aLNP-ECR

We prepared lipid nanoparticle (LNP) using the classical SM102 based ionizable lipid formulation [45]. The components and molar ratios used for unmodified LNP preparation were SM102: cholesterol: DSPC: DMG-PEG2000 = 50:38.5:10:1.5. SM102, cholesterol, DSPC, and DMG-PEG2000 were all purchased from Avanti Polar Lipids (China) to form the organic phase. mRNA was dissolved in citrate buffer (pH 4.0, RNase-free) at a concentration of 1 mg/mL to serve as the aqueous phase. The aqueous and organic phases were mixed at a 3:1 (volume) using syringe pumps in a microfluidic chip device to generate LNP-ECR. The resulting LNP-ECR were dialyzed against phosphate-buffered saline (PBS; pH 7.4) for 12 hours to remove ethanol. Two additional isoforms of LNP-ECR, designated LNP-ECR(ΔGla), LNP-ECR(ΔMertk), were also developed, differing solely in their mRNA sequences.

For anti-Ly6c/LNP-ECR (aLNP-ECR) synthesis, we first prepared LNP-ECR as described above, with the addition of DSPE-PEG2k-mal (UTGene Co., Ltd, China) to enable antibody conjugation. SM102, cholesterol, DSPC, DMG-PEG2000, and DSPE-PEG2k-mal, were dissolved in ethanol at a ratio of 50:38.5:10:1.5: 0.5 to form the organic phase. The mRNA was dissolved in citrate buffer to serve as the aqueous phase. The aqueous and organic phases were mixed at a 3:1 (volume) ratio using syringe pumps via a microfluidic chip system. Secondly, Ly6c antibody (BioXcel, USA) was thiolated using a Protein N-succinimidyl S-acetylthioacetate (SATA) Modification Kit (Thermo Fisher Scientific, USA) according to the manufacturer's instructions. Briefly, Ly6c antibody was dissolved in Reaction Buffer to a final concentration of 60 μM. Prior to the reaction, 8 mg SATA was dissolved in dimethyl sulfoxide (DMSO) to at 55 mM. To modify the antibody, 1.0 mL Ly6c antibody solution was mixed with 10 μL SATA solution and incubated at room temperature for 30 min. The reaction mixture (1.01 mL) was then applied to a pre-equilibrated desalting column (Thermo Fisher Scientific, USA) that had been washed with 10 mL Reaction Buffer. The first 1 mL flow-through was collected, followed by a second 1 mL fraction after additional Reaction Buffer was added and the sample had fully entered the column bed. Next, 1.0 mL SATA-modified Ly6c antibody was mixed with 100 μL deacetylation solution and incubated at room temperature for 2 h. The deacetylated (thiol-exposed) Ly6c antibodies were further purified using a desalting column equilibrated in deacetylation solution and finally exchanged into Reaction Buffer containing 10 mM ethylenediaminetetraacetic acid (EDTA). Finally, for conjugation of LNP-ECR with Ly6c antibody to obtain aLNP-ECR, LNP-ECR and thiolated Ly6c antibody (4:1 mass ratio) were mixed at a 4:1 mass ratio by gentle inversion or pipetting and incubated at room temperature for 1 h, with 2–3 gentle inversions during incubation while monitoring for visible precipitation. The conjugated nanoparticles were purified using 300 kDa ultrafiltration devices (centrifuge speed not exceeding 3900 g), diluted 3–5 fold with PBS, and centrifuged. This dilution and centrifugation process were repeated 3–5 times, with a total buffer exchange of greater than 100-fold (yield calculated as 60% and concentrated accordingly). The final aLNP-ECR formulation was sterilized by filtration through a 0.22 μm membrane.

The morphology of LNP-ECR and aLNP-ECR was observed using transmission electron microscope (JEOL, Japan) operated at 300 kV. The particle size, polydispersity index (PDI), and zeta potential of LNP-ECR and aLNP-ECR were characterized using a Malvern Zetasizer Nano ZS90 (Malvern, UK). Encapsulation efficiency was determined using the Quant-iT RiboGreen assay kit (Thermo Fisher Scientific, USA). To evaluate the storage stability of aLNP-ECR at 4°C, the average particle size, zeta potential, and encapsulation efficiency were monitored over 7 days. Conjugation of Ly6c antibody on the surface of LNP-ECR and aLNP-ECR lipid nanoparticles was verified using nano-flow cytometry.

To assess mRNA degradation in serum-containing medium, 100 μL of Dulbecco's Modified Eagle's Medium (DMEM; Gibco, USA) supplemented with 10% fetal bovine serum (FBS) was added to 10 μL samples containing 50 pmol of either free mRNA or anti-Ly6c/LNP-ECR encapsulated mRNA. The mixtures were incubated at 37°C for various time intervals. Sample preparation and subsequent procedures were performed as described above. Each sample was mixed with DNA loading buffer (Beyotime, China) and loaded onto a 1.5% agarose gel (BIOWEST, France) containing Gel Red nucleic acid stain (Beyotime, China). Electrophoresis was conducted in 1× Tris-acetate-EDTA (TAE) buffer (Sangon Biotech, China) at 120 V for 20 minutes. Gels were visualized using a Bio-Rad ChemiDoc imaging system (Bio-Rad, USA).

4.3 Cell Isolation and Culture

The preparation of bone marrow-derived macrophages (BMDMs) was conducted as previously described [46]. Briefly, BMDMs were harvested from the femurs and tibias of C57BL/6J mice using a sterile 1 mL syringe and PBS. After red blood cell lysis with Hybrid-Max buffer (SIGMA, USA), cells were cultured in DMEM (Gibco, USA) supplemented with 10% FBS (Gibco, USA), 1% penicillin/streptomycin (Gibco, USA), and 20 ng/mL M-CSF (BioLegend, USA). The culture medium was replaced on day 3, and cells are allowed to differentiate for 5–7 days. Subsequently, the preparation of Bone Marrow Mononuclear Cells (BMMNCs) was also performed as previously described [47]. Briefly, single-cell suspensions were collected from the femurs and tibias of C57BL/6J mice using a sterile 1 mL syringe and PBS. The suspension was gently layered onto 3 mL of Ficoll (1x) solution and centrifuged, the buffy coat layer was collected, followed by red blood cell lysis with Hybrid-Max buffer (SIGMA, USA). The resulting cells were cultured in RPMI 1640 supplemented with 10% FBS (Gibco, USA), 1% penicillin/streptomycin (Gibco, USA), and 20 ng/mL M-CSF (BioLegend, USA), BMMNCs were obtained after 2–3 days of culture. The successful extraction of BMDMs and BMMNCs was confirmed by flow cytometry. Peripheral blood mononuclear cells (PBMCs) were isolated from human blood samples. All samples were obtained with informed consent from patients and were ethically approved by the Institutional Review Board of Zhongshan Hospital, Shanghai. Monocytes/macrophages were enriched using CD14 + microbeads (Miltenyi Biotec, Germany) and further purified by cell adhesion for 4 hours. The isolated monocytes/macrophages were cultured in RPMI 1640 medium supplemented with 10% FBS (Gibco, USA), 1% penicillin/streptomycin (Gibco, USA), and 20 ng/mL M-CSF (BioLegend, USA) for 6 days. The successful extraction of human macrophages was confirmed by flow cytometry. Inflammatory BMDMs were induced by stimulating mature BMDMs with 100 ng/mL lipopolysaccharide (LPS, SIGMA, USA) and

20 ng/mL interferon-γ (IFN-γ, PeproTech, USA) for 24 hours. Mouse atrial cardiomyocytes (HL-1, ATCC) were cultured in DMEM supplemented with 10% fetal FBS and 1% penicillin/streptomycin. All cells were maintained at 37°C in a humidified incubator with 5% CO_2 (Thermo Fisher Scientific, USA).

4.4 Generation of ECR-M and mRNA Transfection in vitro

After isolation, BMDMs were seeded into 6-well plates and incubated for 24 hours with GFP encoding mRNA-loaded LNP-ECR at different mRNA doses (0.5, 1, 1.5, 2, or 5 μg per well). Cells were then imaged by Confocal Laser Scanning Microscopy (CLSM; Olympus, Japan). In addition, BMDMs were incubated with GFP mRNA-loaded LNP-ECR (1.5 μg mRNA per well) for 12, 24, 36, or 48 hours, and the GFP fluorescence intensity was observed by CLSM. In both experiments, GFP fluorescence intensity was quantified using ImageJ software. After establishing the optimal conditions for transfection time and dosage, we further evaluated the delivery efficiency of different mRNA sequences. BMDMs were incubated with LNP, naked mRNA and LNP-ECR (1.5 μg mRNA per well) for 24 hours. GFP fluorescence intensity was visualized using CLSM and quantified using ImageJ. Next, the mRNA expression levels were measured using real-time quantitative reverse transcription polymerase chain reaction (RT-qPCR). Total RNA was extracted using Trizol reagent (Invitrogen, USA) according to the manufacturer's instructions. An aliquot of 500 ng total RNA was reverse-transcribed into complementary DNA (cDNA) using the PrimeScript RT Master Mix (TaKaRa, Japan) with the following program: 37°C for 60 minutes, 95°C for 3 minutes, then held at 4°C. The cDNA was used as template for RT-qPCR with SuperReal Premix Plus SYBR Green (TIANGEN, China) on a CFX96 Real-Time PCR Detection System (Bio-Rad, USA). The cycling conditions were: initial denaturation at 95°C for 15 minutes, followed by 40 cycles of 94°C for 20 seconds and 60°C for 30 seconds. The expression levels were normalized to β-actin, and relative quantification was calculated using the $2^{-\Delta\Delta Ct}$ method. Primer sequences for mouse genes used in this study are listed in Supplementary Table 3.

In vitro, ECR-M were generated by incubating macrophages with LNP-ECR, and ECR expression in these macrophages was subsequently analyzed. BMDMs were incubated with LNP, mRNA, and LNP-ECR, respectively. After 24 hours of incubation, the percentage of GFP-positive and Flag-positive cells were determined by flow cytometry. For flow cytometry, cells were digested with 0.25% trypsin (Gibco, USA) and collected by centrifugation at 1000 rpm for 5 min. A total of 1×10^6 cells was resuspended in 100 μL staining buffer (Well Biotech, China) and incubated with an APC-anti-DYKDDDDK Tag (BioLegend, USA) for 40 min at room temperature. Unbound antibody was removed by centrifugation, and cells were resuspended in staining buffer for acquisition. All samples were analyzed within 1 h on a BD FACSAria III flow cytometer (BD Biosciences, USA). GFP mean fluorescence intensity (MFI) was quantified using FlowJo v10 (FlowJo, USA). Then, the expression of Flag tag in BMDMs was analyzed by Western blot (WB). Briefly, all samples were separated by electrophoresis on a 10% SDS-polyacrylamide gel (Bio-Rad, USA), and then transferred to polyvinylidene difluoride (PVDF) membranes. The membranes were probed with specific antibodies against Flag (Proteintech, USA), followed by incubation with horseradish peroxidase (HRP) secondary antibodies (Biotech Well, China) corresponding to the host species of the

primary antibodies. Protein bands were visualized using the Bio-Rad ChemiDoc imaging system (Bio-Rad, USA).

4.5 Macrophages-Targeted and Endolysosomal Escape in vitro

Firstly, BMDMs were activated to a pro-inflammatory state as previously described. DiD dye was dissolved in the ethanol phase to prepare DiD-labeled lipid nanoparticle. The activated BMDMs were then incubated for 30 mins with PBS, DiD (on the LNP) labeled LNP-ECR, aLNP-ECR or aLNP-ECR preincubated with anti-Ly6c antibody for blocking (BioXcel, USA). The interactions between lipid nanoparticles and cells were subsequently analyzed using immunofluorescence assay and flow cytometry. For immunofluorescence assays, cells were washed three times with PBS and fixed with 4% paraformaldehyde (Beyotime, China) for 20 min. After fixation, cells were blocked with 3% BSA solution for 1 hour and incubated overnight at 4°C with primary antibody Rat-anti-PSGL-1 (Santa Cruz, USA). After three additional PBS washes, cells were stained with the secondary antibody Alexa Fluor 488-anti-Rat (Abcam, Japan). Nuclei were counterstained with DAPI (Beyotime, China). Fluorescent signals were detected using a CLSM. Flow cytometry analysis was performed as described above and the MFI of DiD signals was determined using FlowJo V10 software.

After pro-inflammatory activation, BMDMs were treated with FAM (on mRNA) labeled aLNP-ECR at 37°C for 0.5, 3, and 6 hours. LysoTracker Red (Beyotime, China) was used to stain lysosomes, and Hoechst 33342 (Beyotime, China) was used for nuclear staining. Cells were then imaged by CLSM to assess intracellular trafficking and colocalization.

4.6 ECR-M Functional Analysis in virto

Firstly, we assessed the phagocytic activity associated with ECR and its isoforms. HL-1 cardiomyocytes were labeled with IVISense 680 fluorescent dye (PerkinElmer, USA) and induced to undergo apoptosis using 5 μM staurosporine (Med Chem Express, USA). The apoptotic cardiomyocytes were then co-incubated with the pretreated BMDMs for 45 minutes. After incubation, unbound apoptotic cardiomyocytes were removed. The co-localization of macrophages and cardiomyocytes was observed using CLSM to assess the phagocytic capability of macrophages in each group. The phagocytosis rate was calculated as the percentage of macrophages that had engulfed or were associated with cardiomyocytes among the total macrophage population. Macrophage cell membranes were then labeled with

Texas-Red-labeled wheat germ agglutinin (WGA). DAPI (Beyotime, China) was used as a nuclear stain. Similarly, flow cytometry analysis was performed as described above after cell collection. FITC-anti-CD45, PerCP-Cy5.5-anti-CD11b and PE-anti-F4/80 (all from eBioscience, USA) were used in this experiment. Then, we employed Western blot to examine the levels of Gla carboxylation and Mertk phosphorylation in macrophages subjected to five different treatments. BMDMs were pretreated with LNP-ECR(ΔGla), LNP-ECR(ΔMertk), LNP-ECR, Annexin (Med Chem Express, USA) or Mertk inhibitor

(Selleckchem, USA). The amount of ECR added was standardized based on the Flag tag content. Subsequently, the carboxylated Gla (c-Gla) and phosphorylated Mertk (p-Mertk) were were detected by western blotting and quantified using ImageJ, following the procedures as described previously. The antibodies used included c-GLA (TakaRa, Japan) and p-Mertk (STARTER, China), along with their corresponding secondary antibodies. Then Rac1 activation in BMDMs was assessed using a PAK p21-binding domain (PAK-PBD) pull-down assay. Briefly, BMDMs were subjected to the indicated treatments and then lysed on ice in lysis buffer containing 50 mM Tris-HCl (pH 7.5), 150 mM NaCl, 10 mM $MgCl_2$, 1% Nonidet P-40, 10% glycerol, supplemented with protease and phosphatase inhibitor cocktails (Beyotime, China). Cell lysates were incubated on ice for 15–30 min with intermittent gentle pipetting and then clarified by centrifugation at 12,000g for 10 min at 4°C to obtain the supernatants (total cell lysates). GTP-bound active Rac1 was isolated using agarose beads conjugated with the PAK-PBD (Beyotime, China) according to the manufacturer's instructions. Equal amounts of protein from each sample (500μg) were incubated with pre-equilibrated PAK-PBD agarose beads at 4°C for 1 hour with gentle rotation. After incubation, the beads were collected by centrifugation at 5000g for 1 min at 4°C and washed three times with ice-cold lysis buffer to remove non-specifically bound proteins. Bound proteins were eluted by boiling the beads in 2× SDS sample buffer at 95°C for 5 min. Eluted proteins were resolved by SDS-PAGE and transferred onto PVDF membranes, followed by immunoblotting with an anti-Rac1 antibody (Beyotime, China), which was also used to determine total Rac1 levels in aliquots of input lysates. Bands were visualized by enhanced chemiluminescence and quantified by densitometric analysis using ImageJ. In addition, RT-qPCR was performed to assess key downstream molecules in the Mertk signaling pathway, including PI3K, AKT, and ERK. RT-qPCR experiments were conducted according to the same protocol as described above, and the sequences of the mouse gene primers used in this study are listed in Supplementary Table 3.

Next, we assessed the impact of aLNP-ECR on macrophages phagocytic activity. BMDMs were pretreated with LNP-mRNA, aLNP-mRNA, LNP-ECR, or aLNP-ECR. The procedures for immunofluorescence and flow cytometry were consistent with those described above.

The in vitro phenotype of ECR-M was validated using flow cytometry and immunofluorescence staining. The experimental procedures were performed as described above. For flow cytometry, cells were incubated with PE-Cy7-anti-CD86 (eBioscience, USA) and APC-anti-CD206 (eBioscience, USA). Immunofluorescence staining was carried out using Mouse anti-iNOS antibody (Invitrogen, USA), Alexa Fluor 647-anti-CD206 antibody (BioLegend, USA), and Alexa Fluor 568-anti-mouse secondary antibody (Abcam, Japan). The stained cells were analyzed using the corresponding detection platforms.

The mRNA expression levels of M1 markers (iNOS, IL-1β and IL-6) and M2 markers (Arg-1, IL-10, and YM-1) were assessed by RT-qPCR. Total RNA was extracted as described above. cDNA synthesis was performed using PrimeScript RT Master Mix (TaKaRa, Japan), and RT-PCR amplification was carried out with SuperReal Premix Plus-SYBR Green (TIANGEN, China). The RT-qPCR procedures followed the protocols described previously. Primer sequences for mouse genes used in this study are listed in Supplementary Table 3.

4.8 Animals

Eight-week-old male C57BL/6J mice used in this study were purchased from Shanghai JieSiJie Laboratory Animal Co., Ltd. The mice were housed in a temperature-controlled environment (22°C) under a 12-hour light/12-hour dark cycle, with free access to standard laboratory chow and tap water. All animal experiments were approved by the Ethics Committee of Zhongshan Hospital, Fudan University, Shanghai, China, and were conducted in strict accordance with the Guidelines for the Care and Use of Laboratory Animals published by the Institute of Laboratory Animal Research of the National Research Council (USA).

4.9 Myocardial Ischemia-Reperfusion Injury Animal Model

The mice model of myocardial ischemia-reperfusion (MI/R) injury was established by ligating the left anterior descending (LAD) coronary artery for 60 minutes, followed by reperfusion. Successful induction of myocardial injury was confirmed by electrocardiographic ST-segment changes and alterations in the color of the left ventricle.

4.10 Biodistribution and Targeting Specificity of aLNP-ECR in vivo

DiD dye was dissolved in the ethanol phase to prepare DiD-labeled lipid nanoparticle for evaluating the biodistribution of aLNP-ECR in mice. MI/R mice were intravenously injected via the tail vein with 200 μL PBS, DiD (on the LNP) labeled LNP-ECR, or aLNP-ECR, respectively. At three predetermined time points after administration (3, 24, and 72 hours), major organs (heart, liver, spleen, lungs, kidneys, and brain) were harvested and subjected to ex vivo imaging using an in vivo imaging system (IVIS, PerkinElmer, USA) to assess aLNP-ECR distribution. At 24 hours post-administration, the distribution of LNP in the injured heart was further assessed by immunofluorescence staining. Briefly, the injured hearts were collected and embedded in optimal cutting temperature compound (OCT, Sakura Finetek, Japan), followed by rapid freezing in liquid nitrogen and sectioning into 8-μm-thick cryo-sections. The sections were either stained immediately or stored at -20°C for later use. For immunofluorescence staining, tissue sections were first fixed in acetone for 20 minutes and washed three times with PBS, followed by blocking with 3% BSA for 1 hour. Sections were then incubated overnight at 4°C with Rabbit anti-cardiac troponin T primary antibody (ProteinTech, USA). The next day, after three PBS washes, the sections were incubated for 1 hour with an Alexa Fluor 488-anti-Rabbit secondary antibody (Abcam, Japan), and nuclei were counterstained with DAPI.

To further investigate the accumulation of lipid nanoparticles in circulating $Ly6c^+$ monocytes and cardiac $F480^+$ macrophages, flow cytometry analysis was performed. MI/R-induced C57BL/6 mice were randomly divided into two groups and intravenously injected with 200 μL of DiD-labeled LNP-ECR or aLNP-ECR at 24 hours post-injury. One day after injection, blood samples were collected via the orbital sinus and stained with specific antibodies: FITC-anti-CD45 (eBioscience, USA), PerCP-Cy5.5-anti-CD11b (eBioscience, USA), and PE-Cy7-anti-Ly6C (BD Pharmingen, USA). Red blood cells were lysed with RBC

Lysis Buffer (Invitrogen, USA) for 5 minutes. After centrifugation at 1000 rpm for 5 minutes, the cells were resuspended in staining buffer and analyzed for fluorescence signals using a BD FACS Aria III flow cytometer. In addition, to obtain single-cell suspensions of cardiomyocytes from the infarct region, the Multi Tissue Dissociation Kit 2 (Miltenyi Biotec, USA) was used according to the manufacturer's instructions. Briefly, infarcted myocardium was cut into small pieces (1 mm^3) and digested in an enzyme mixture at 37°C for 15 minutes. The samples were then mechanically dissociated using the gentle MACS Dissociator (Miltenyi Biotec, USA) with the "Multi_G" program, and this process was repeated once. After filtration through a MACS SmartStrainer (70 μm), the resulting cell suspension was centrifuged at 600 g for 5 minutes to isolate single cells. The cell pellet was resuspended in 200 μL of staining buffer. Subsequent staining and detection procedures were performed as described above, using the following specific primary antibodies: FITC-anti-CD45 (eBioscience, USA), PerCP-Cy5.5-anti-CD11b (eBioscience, USA), and PE-anti-F4/80 (eBioscience, USA). Immunofluorescence staining was also performed to analyze the colocalization of lipid nanoparticles and monocytes/macrophages in the injured area. The staining procedure was the same as described above, except that Rat anti-CD11b antibody (Abcam, Japan) and Alexa Fluor 488-anti-Rat secondary antibody (Abcam, Japan) were used. Fluorescence signals were detected using a CLSM, and colocalization analysis between DiD signals and CD11b + cells were performed using ImageJ.

Flow cytometry was subsequently used to verify in vivo expression of ECR. MI/R-induced C57BL/6 mice were randomly divided into three groups and intravenously injected with 200 μL of PBS, DiD-labeled LNP-ECR, or aLNP-ECR at 24 hours post-injury. The collection of mouse blood and preparation of single-cell suspensions were performed as previously described. Blood samples were stained with the following specific antibodies: FITC-anti-CD45 (eBioscience, USA), PerCP-Cy5.5-anti-CD11b (eBioscience, USA) and PE-Cy7-anti-Ly6c (BD Pharmingen, USA). For cardiac single-cell suspensions, the following antibodies were used: FITC-anti-CD45 (eBioscience, USA), PerCP-Cy5.5-anti-CD11b (eBioscience, USA) and PE-anti-F4/80 (eBioscience, USA). The GFP MFI was quantified using FlowJo v10 (FlowJo, USA).

4.11 Cardiac Function Measurement

C57BL/6 mice were randomly divided into a sham-operated group and four MI/R groups. MI/R mice received tail vein injections of 200 μL of LNP-mRNA, aLNP-mRNA, LNP-ECR, or aLNP-ECR on the one day after surgery. One day post-injection of the drug, the hearts were excised and subsequently frozen at -40°C for future slicing. Each heart was then sectioned into five pieces (1mm thickness) and washed with ice-cold PBS. The sections were incubated in a 1% TTC PBS solution at 37°C for 20 minutes, after which 4% PFA was added to stop the reaction and fix the tissue. The stained slices were scanned using an EPSON Perfection V19 scanner, and analysis was conducted with Image-Pro Plus 6.0.

At the indicated time points, cardiac geometry and function were assessed by two-dimensional guided M-mode echocardiography using a Visual Sonics Vevo 770 system (VisualSonics, Canada). After hair removal, mice were anesthetized with a controlled flow of isoflurane to maintain a heart rate of approximately 450 beats per minute. LVEF, fractional shortening, LVESV, and LVEDV were measured. The

echocardiographer was blinded to the treatment groups, and all measurements were averaged over six consecutive cardiac cycles.

Subsequently, the hearts were excised and fixed overnight in 4%PFA, embedded in paraffin, and sectioned continuously at a thickness of 3 μm. The sections were then stained with hematoxylin and eosin (H&E) to evaluate pathological injury, and with Masson's trichrome to assess infarct location and size. Infarct area was quantified using ImageJ software.

4.12 Cardiac phagocytosis in vivo

To assess the phagocytic capacity of ECR-M in the injured heart, α-MHCCre: Rosa26-tdTomato mice were used, in which cardiomyocytes are specifically labeled with red fluorescence (tdTomato). When cardiomyocytes are phagocytosed by macrophages, the tdTomato signal can be detected within the macrophages. The tdTomato-positive ($tdTomato^+$) signal in ECR-M was detected by flow cytometry. αMHC-Cre: Rosa26-tdTomato mice were subjected to MI/R surgery. On the first day after surgery, mice were intravenously injected via the tail vein with 200 μL LNP-mRNA, aLNP-mRNA, LNP-ECR, or aLNP-ECR. Three days following drug administration, flow cytometry analysis was performed. Cardiac single-cell suspensions were prepared as described previously. The following antibodies were used for staining: FITC-anti-CD45 (eBioscience, USA), PerCP-Cy5.5-anti-CD11b (eBioscience, USA), and PE-anti-F4/80 (eBioscience, USA). Immunofluorescence staining was further used to evaluate phagocytic activity within the injured myocardium. As previously described, apoptotic cardiomyocytes exhibited tdTomato red fluorescence. CLSM was utilized to visualize the co-localization of macrophages and apoptotic cardiomyocytes, enabling precise evaluation of phagocytosis. Quantitative analysis of the phagocytic ratio was subsequently performed to systematically determine the extent to which ECR-M engulfed the apoptotic cardiomyocytes within the affected cardiac tissue.

To evaluate the efficiency of apoptotic cell clearance in MI/R hearts, Tunel staining was performed after different treatments. Mice were subjected to MI/R surgery. On the first day post-operation, mice received an intravenous injection of 200 μL of LNP-mRNA, aLNP-mRNA, LNP-ECR, or aLNP-ECR via the tail vein. Three days after drug administration, hearts were harvested, and prepared as frozen sections according to standard protocols. Tunel staining was performed on heart cryo-sections according to the manufacturer’s instructions, and DAPI was used as a nuclear counterstain. The proportion of Tunel + cells was then quantified to assess apoptotic cell burden in the infarcted myocardium.

4.13 ECR-M Functional Analysis in vivo

Western blotting was performed to assess the phosphorylation level of Mertk in infarcted heart tissue. Heart tissues from the four different treatment groups were collected from the damaged regions and mechanically homogenized in lysis buffer containing RIPA buffer (1x) and phosphatase inhibitors (1x). The homogenate was then centrifuged at 12,000 rpm for 15 minutes at 4°C. The supernatant, which contains the extracted proteins, was carefully collected and transferred to a clean microcentrifuge tube for further analysis. Phosphorylated Mertk protein was detected using an anti-p-Mertk antibody (STARTER, China) and the corresponding secondary antibody. Additionally, RT-qPCR was conducted to

detect key molecules in the downstream pathways of Mertk, including PI3K, AKT, and ERK. The experimental procedures for RT-qPCR were performed according to the methods described above. The sequences of the mouse gene primers used in this study are detailed in Supplementary Table 3.

4.14 Immunoregulatory effects of aLNP-ECR in vivo

Mice were subjected to MI/R surgery and treated with 200 μL of LNP-mRNA, aLNP-mRNA, LNP-ECR, or aLNP-ECR. Three days after administration, flow cytometry was performed to assess the inflammatory phenotypes of macrophages. All experimental procedures were performed as previously described. The following antibodies were used: FITC-anti-CD45 (eBioscience, USA), PerCP-Cy5.5-anti-CD11b (eBioscience, USA), PE-anti-F4/80 (eBioscience, USA), PE-Cy7-anti-CD86 (eBioscience, USA), and APC-anti-CD206 (eBioscience, USA).

After treatment with LNP-mRNA, aLNP-mRNA, LNP-ECR, or aLNP-ECR for three days, the levels of inflammation-related cytokines (TGF-β, IL-10, IL-1β and TNF-α), and SPMs (RvD1, RvD2, RvE1, and LXA4) in myocardial tissue homogenates were determined by ELISA. ELISA kits for TGF-β, IL-10, IL-1β and TNF-α were purchased from Biolegend (USA). Resolvin D1 and Resolvin D2 ELISA kits were obtained from Cayman (USA), the Resolvin E1 ELISA kit was purchased from TW-Reagent (China), and the lipoxin A4 ELISA kit was obtained from Elabscience (China). All assays were performed according to the manufacturers' instructions.

4.15 Bulk RNA-seq data processing and analysis

Total RNA was isolated from BMDMs or mouse heart injury area using the Trizol Reagent (Invitrogen Life Technologies, USA), after which the concentration, quality and integrity were determined using a NanoDrop spectrophotometer (Thermo Scientific, USA). Total RNA was used to construct poly(A)-selected mRNA libraries using the NEBNext Ultra II RNA Library Prep Kit for Illumina (New England Biolabs Inc., USA). Library quality was assessed with the Agilent 2100 Bioanalyzer (Agilent Technologies Inc., USA) and Agilent High Sensitivity DNA Kit (Agilent Technologies Inc., USA). Qualified libraries were sequenced on an Illumina platform in the PE150 mode. Raw reads were subjected to quality control using Fastp (v0.22.0) to remove sequencing adaptors, trim 3' end adaptors, and eliminate reads with an average quality score below Q20. Clean reads were mapped to the reference genome, and HTSeq (v0.9.1) was used to count the number of mapped reads for each gene. Gene expression levels were normalized as FPKM (Fragments Per Kilobase of transcript per Million fragments mapped) to account for variability in transcript length and sequencing depth among genes and samples. Differential expression analysis was performed using DESeq (v1.38.3). Differentially expressed genes (DEGs) were defined as those with $|log2FoldChange| > 1$ and $P\text{-value} < 0.05$. KEGG pathway enrichment analysis of DEGs was carried out using clusterProfiler (v4.6.0), with significance determined by hypergeometric testing at $P\text{-value} < 0.05$, to identify the major biological functions and pathways associated with the DEGs.

4.16 Analysis of public RNA-seq data

The public single-cell sequencing data are available on cellxgene (https://cellxgene.

cziscience.com/collections/8191c283-0816-424b-9b61-c3e1d6258a77) and in the Zenodo data repository (https://zenodo.org/record/6578047), and the publicly available bulk transcriptome sequencing data GSE214611 were processed and analyzed using the following methods. The original gene expression matrices processed using the Seurat package (v5.3.1). Cells were first filtered according to quality control (QC) metrics, then normalized using the LogNormalize method and scaled. The top 2,000 highly variable features were selected for principal component analysis (PCA). Based on the first 30 principal components (PCs), unsupervised clustering was performed using the Leiden algorithm (via the FindClusters function), and dimensionality reduction for visualization was done with UMAP. Cell type annotation was completed using marker genes identified by FindAllMarkers and canonical markers. To characterize shifts in cellular functional states, pathway enrichment scores were calculated using UCell (v2.8.0). This study constructed custom gene sets (gene signatures) covering phagocytosis and fibrosis.

4.17 Single-cell RNA-seq

Single cells were counted and quality-controlled using a TC20 automated cell counter (Bio-Rad, USA). After gel bead-in-emulsion (GEM) generation, full-length cDNA amplification products containing 10x barcodes were obtained from polyadenylated mRNA. After library construction, all libraries with different indices were pooled and sequenced according to the manufacturer's instructions (Illumina NovaSeq, Illumina, San Diego, CA, USA). Quality control and alignment of the raw sequencing data were performed using 10X Genomics' single-cell gene expression pipeline. Cell quality control, clustering, and marker gene analysis were then performed using Seurat (v4.1.1). We excluded genes expressed in very few cells to preserve gene and cell quality. Cell type annotation was performed using SingleR (v1). GO and KEGG enrichment analyses were performed using clusterProfiler, Reactome pathway enrichment was performed with reactomePA (v1.42.0), and gene set variation analysis (GSVA) was performed using GSVA (v1.42.0). In addition, Monocle was used to infer cellular pseudotime trajectories, and CellChat was used to infer cell–cell communication.

4.18 Biosafety Evaluation of aLNP-ECR

In vitro, the cytotoxicity of aLNP-ECR to BMDMs was assessed using a CCK-8 assay kit (Beyotime, China) according to the manufacturer’s instructions. Absorbance at 450 nm was measured using an EPOCH 2 microplate reader (BioTek, USA).

For in vivo biosafety evaluation, healthy mice were randomly divided into groups and administered 200 μL of aLNP-ECR or PBS. Four weeks later, serum levels of the inflammatory cytokine TNF-α and IL-1β, as well as total antibodies IgG and IgM, were quantitatively measured using ELISA kits (Biolegend, USA) following the manufacturer’s instructions. Biochemical assays were performed to assess liver function (AST, ALT) and kidney function (CREA, UREA) in mice serum. Coagulation function was analyzed using citrated whole blood to measure APTT, PT and Fbg. Major organs, including brain, liver, spleen, lung, and kidney, were then collected and evaluated by H&E staining.

4.19 Statistical Analysis

All quantitative data are presented as the mean ± standard deviation (SD) from three or four independent in vitro replicates or six in vivo replicates. Comparisons between two groups were performed using two-tailed Student's t-tests. Statistical analysis among multiple groups was conducted using one-way analysis of variance (ANOVA) followed by Bonferroni's post hoc test. Differences between groups were considered not significant (^{NS}P), significant when *P < 0.05, highly significant when **P < 0.01, and extremely significant when *P < 0.001. Statistical and graphical analyses were performed using SPSS Statistics 26.0 (IBM, USA) and GraphPad Prism 7.0 (GraphPad Software, USA), respectively.

Declarations

6. Conflict of Interest

The authors declare no conflict of interest.

Acknowledgements

We acknowledge support from the National Natural Science Foundation of China (82470263, 82170254, 82370257), Shanghai Rising-Star Program (23QA1401300)and Chongqing Postdoctoral Innovative Talent Support Program (CQBX202427).

7. Data Availability Statement

The data that support the findings of this study are available from the corresponding author upon reasonable request.

References

1. RURIK JG, AGHAJANIAN H (2021) Immune Cells and Immunotherapy for Cardiac Injury and Repair [J]. Circ Res 128(11):1766–1779
2. SUN K, LI Y Y JINJ (2021) A double-edged sword of immuno-microenvironment in cardiac homeostasis and injury repair [J]. Signal Transduct Target Ther 6(1):79
3. ANDREADOU I, GHIGO A, NIKOLAOU P E et al (2025) Immunometabolism in heart failure [J]. Nat Rev Cardiol
4. PRABHU SD, FRANGOGIANNIS N G (2016) The Biological Basis for Cardiac Repair After Myocardial Infarction: From Inflammation to Fibrosis [J]. Circ Res 119(1):91–112

5. HEUSCH G. Myocardial ischaemia-reperfusion injury and cardioprotection in perspective [J]. Nat Rev Cardiol, (2020) 17(12): 773–789
6. FERDINANDY P, ANDREADOU I, BAXTER G F et al (2023) Interaction of Cardiovascular Nonmodifiable Risk Factors, Comorbidities and Comedications With Ischemia/Reperfusion Injury and Cardioprotection by Pharmacological Treatments and Ischemic Conditioning [J]. Pharmacol Rev 75(1):159–216
7. HARRINGTON RA (2017) Targeting Inflammation in Coronary Artery Disease [J]. N Engl J Med 377(12):1197–1198
8. FRANGOGIANNIS N G (2012) Regulation of the inflammatory response in cardiac repair [J]. Circ Res 110(1):159–173
9. DORAN A C, YURDAGUL A (2020) JR., TABAS I. Efferocytosis in health and disease [J]. Nat Rev Immunol 20(4):254–267
10. BOADA-ROMERO E, MARTINEZ J, HECKMANN B, L et al (2020) The clearance of dead cells by efferocytosis [J]. Nat Rev Mol Cell Biol 21(7):398–414
11. MORIOKA S, MAUERÃ¶DER C (2019) RAVICHANDRAN K S. Living on the Edge: Efferocytosis at the Interface of Homeostasis and Pathology [J]. Immunity 50(5):1149–1162
12. HENSON PM (2017) Cell Removal: Efferocytosis [J]. Annu Rev Cell Dev Biol, 33(127 – 44.
13. MEHROTRA P, RAVICHANDRAN KS (2022) Drugging the efferocytosis process: concepts and opportunities [J]. Nat Rev Drug Discov 21(8):601–620
14. ZHANG B, ZOU Y, YUAN Z et al (2024) Efferocytosis: the resolution of inflammation in cardiovascular and cerebrovascular disease [J]. Front Immunol, 15(1485222
15. ZHANG YQ, NIE R, FENG Z Y et al (2025) Efferocytosis in tissue engineering: A comprehensive review of emerging therapeutic strategies for enhanced tissue repair and regeneration [J]. Bioact Mater, 52(155 – 81.
16. WAN E, YEAP X Y, DEHN S et al (2013) Enhanced efferocytosis of apoptotic cardiomyocytes through myeloid-epithelial-reproductive tyrosine kinase links acute inflammation resolution to cardiac repair after infarction [J]. Circ Res 113(8):1004–1012
17. TUTUSAUS A, MARÃ M, ORTIZ-PÃ©REZ JT et al (2020) Role of Vitamin K-Dependent Factors Protein S and GAS6 and TAM Receptors in SARS-CoV-2 Infection and COVID-19-Associated Immunothrombosis [J]. Cells, 9(10)
18. DEBERGE M, YEAP X Y, DEHN S et al (2017) MerTK Cleavage on Resident Cardiac Macrophages Compromises Repair After Myocardial Ischemia Reperfusion Injury [J]. Circ Res 121(8):930–940
19. DICK S A, MACKLIN J A, NEJAT S et al (2019) Self-renewing resident cardiac macrophages limit adverse remodeling following myocardial infarction [J]. Nat Immunol 20(1):29–39
20. ZAGÃ³RSKA A, TRAVÃ©S PG, LEW E D et al (2014) Diversification of TAM receptor tyrosine kinase function [J]. Nat Immunol 15(10):920–928

21. LUMBROSO D, SOBOH S, MAIMON A et al (2020) Corrigendum: Macrophage-Derived Protein S Facilitates Apoptotic Polymorphonuclear Cell Clearance by Resolution Phase Macrophages and Supports Their Reprogramming [J]. Front Immunol, 11(412281
22. DALLI J, SERHAN C N (2012) Specific lipid mediator signatures of human phagocytes: microparticles stimulate macrophage efferocytosis and pro-resolving mediators [J]. Blood 120(15):e60–72
23. SERHAN C N SAVILLJ (2005) Resolution of inflammation: the beginning programs the end [J]. Nat Immunol 6(12):1191–1197
24. CAI B, THORP E B, DORAN A C et al (2016) MerTK cleavage limits proresolving mediator biosynthesis and exacerbates tissue inflammation [J]. Proc Natl Acad Sci U S A 113(23):6526–6531
25. MORIOKA S, KAJIOKA D, YAMAOKA Y et al (2022) Chimeric efferocytic receptors improve apoptotic cell clearance and alleviate inflammation [J]. Cell, 185(26): 4887 – 903.e17.
26. SHAO L, ZHANG Y, YANG Z et al (2025) Synthetic efferocytic receptor microglia enhances anti-inflammatory clearance of amyloid-Î² for AD treatment in mice [J]. Sci Adv 11(28):eads6613
27. LEMKE G. Phosphatidylserine Is the Signal for TAM Receptors and Their Ligands [J]. Trends Biochem Sci, (2017) 42(9): 738–748
28. LINGER R M, KEATING A K, EARP HS et al (2008) TAM receptor tyrosine kinases: biologic functions, signaling, and potential therapeutic targeting in human cancer [J]. Adv Cancer Res 100:35–83
29. SASAKI T, KNYAZEV P G, CHEBURKIN Y et al (2002) Crystal structure of a C-terminal fragment of growth arrest-specific protein Gas6. Receptor tyrosine kinase activation by laminin G-like domains [J]. J Biol Chem 277(46):44164–44170
30. ZHANG W, JIANG Y, HE Y et al (2023) Lipid carriers for mRNA delivery [J]. Acta Pharm Sin B 13(10):4105–4126
31. STITT T N, CONN G, GORET M et al (1995) The anticoagulation factor protein S and its relative, Gas6, are ligands for the Tyro 3/Axl family of receptor tyrosine kinases [J]. Cell 80(4):661–670
32. DRANSFIELD I, ZAGÃ³RSKA A, LEW E D et al (2015) Mer receptor tyrosine kinase mediates both tethering and phagocytosis of apoptotic cells [J]. Cell Death Dis 6(2):e1646
33. HALL A (2012) Rho family GTPases [J]. Biochem Soc Trans 40(6):1378–1382
34. ROTHLIN C V, CARRERA-SILVA E A BOSURGIL et al (2015) TAM receptor signaling in immune homeostasis [J]. Annu Rev Immunol, 33(355 – 91.
35. CULLIS P R, HOPE MJ (2017) Lipid Nanoparticle Systems for Enabling Gene Therapies [J]. Mol Ther 25(7):1467–1475
36. LEMKE G (2013) Biology of the TAM receptors [J]. Cold Spring Harb Perspect Biol 5(11):a009076
37. AGHAJANIAN H, KIMURA T, RURIK J G et al (2019) Targeting cardiac fibrosis with engineered T cells [J]. Nature 573(7774):430–433
38. WANG J, DU H, XIE W et al (2024) CAR-Macrophage Therapy Alleviates Myocardial Ischemia-Reperfusion Injury [J]. Circ Res 135(12):1161–1174

39. VOELKER D R FADOKVA, CAMPBELL P A et al (1992) Exposure of phosphatidylserine on the surface of apoptotic lymphocytes triggers specific recognition and removal by macrophages [J]. J Immunol 148(7):2207–2216
40. FORTE E (2022) The multifaceted effect of efferocytosis on cardiac repair after infarction [J]. Nat Cardiovasc Res 1(4):283
41. CHEN Y, KOU Y, NI Y et al (2025) Microglia efferocytosis: an emerging mechanism for the resolution of neuroinflammation in Alzheimer's disease [J]. J Neuroinflammation 22(1):96
42. TANG X, PENG Y, JIANG Z et al (2025) Efferocytosis and its role in rheumatic diseases [J]. Arthritis Rheumatol
43. TABAS I, BORNFELDT KE (2020) Intracellular and Intercellular Aspects of Macrophage Immunometabolism in Atherosclerosis [J]. Circ Res 126(9):1209–1227
44. ZWOLSMAN R, DARWISH Y B KLUZAE et al (2025) Engineering Lipid Nanoparticles for mRNA Immunotherapy [J]. Wiley Interdiscip Rev Nanomed Nanobiotechnol 17(2):e70007
45. CORBETT K S, EDWARDS D K, LEIST SR et al (2020) SARS-CoV-2 mRNA vaccine design enabled by prototype pathogen preparedness [J]. Nature 586(7830):567–571
46. DE COUTO G, LIU W (2015) Macrophages mediate cardioprotective cellular postconditioning in acute myocardial infarction [J]. J Clin Invest 125(8):3147–3162
47. SWIRSKI F K, LIBBY P (2007) Ly-6Chi monocytes dominate hypercholesterolemia-associated monocytosis and give rise to macrophages in atheromata [J]. J Clin Invest 117(1):195–205

Figures

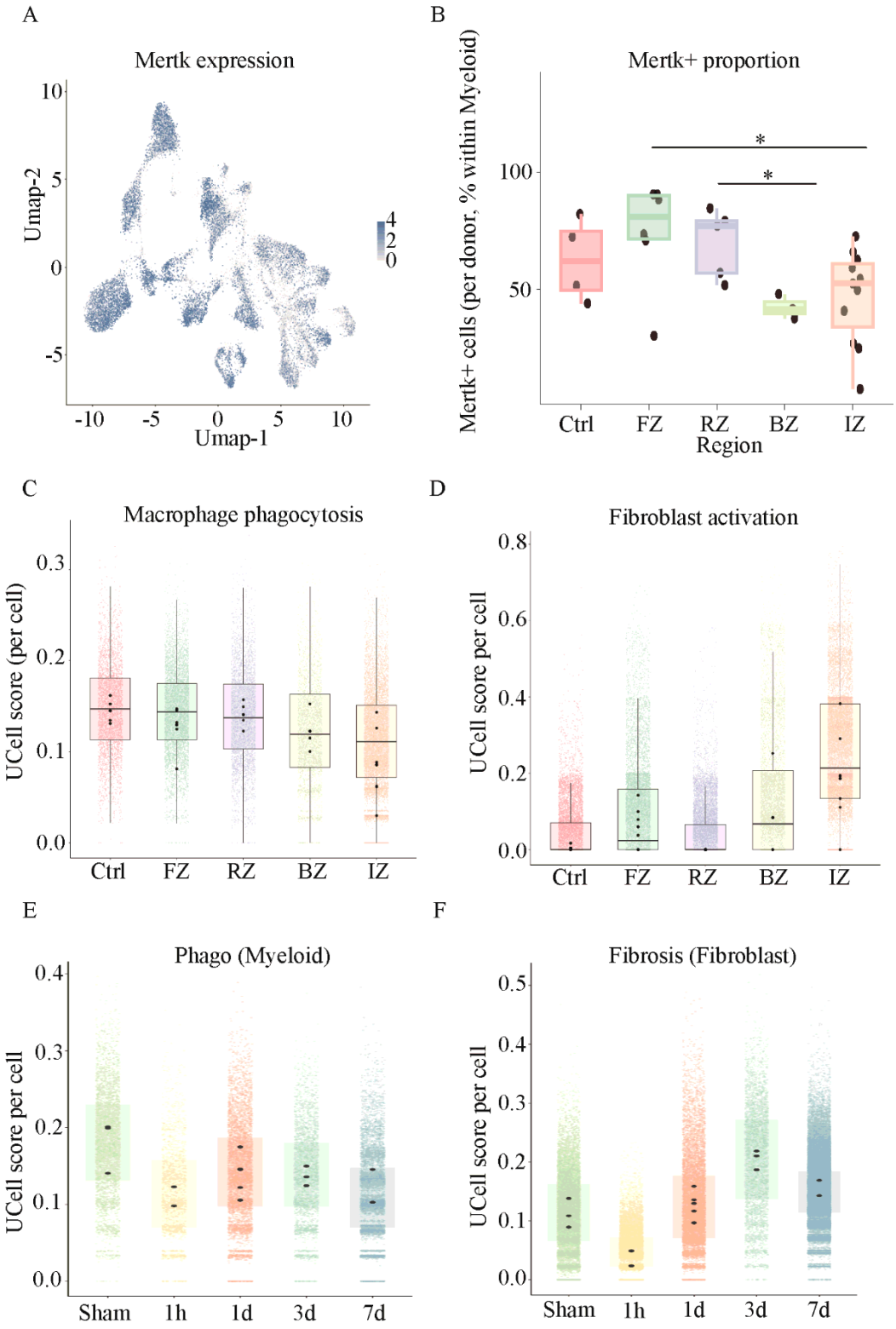


Figure 1

Impaired efferocytosis and fibroblast activation in the infarct zone after MI. (A) Uniform manifold approximation and projection plot (UMAP) feature plot showing Mertk expression within macrophage clusters. (B) Proportion of Mertk-positive macrophages across myocardial regions. Ctrl, healthy donor; FZ, fibrotic zone; RZ, remote zone; BZ, border zone; IZ, infarct zone. (C) Macrophage phagocytic capacity scores across myocardial regions. (D) Fibroblast activation scores across myocardial regions. (E-F)

Temporal changes of macrophage phagocytic capacity (E) and fibroblast activation (F) in mouse MI. Data are presented as mean ± SD. *P < 0.05.

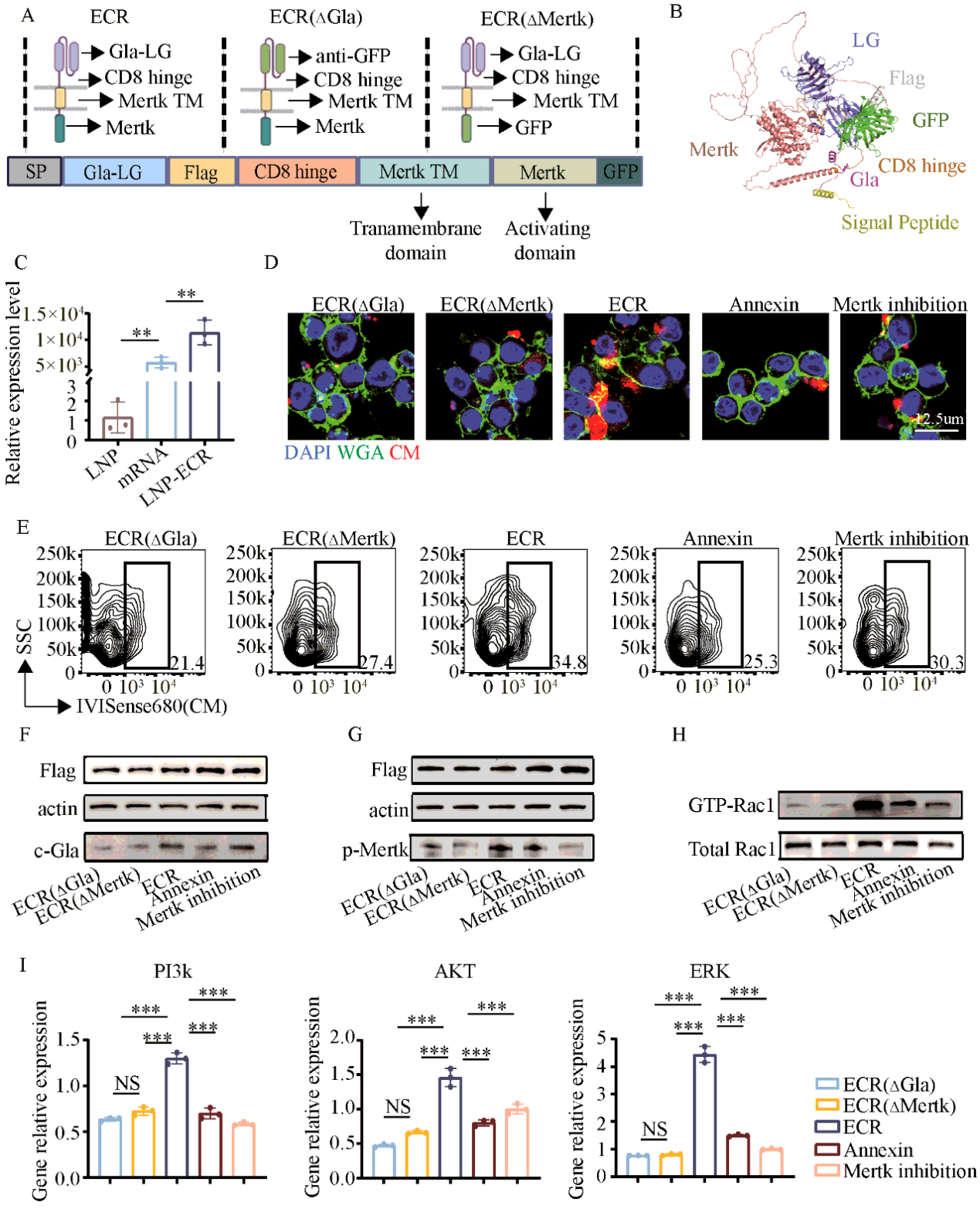


Figure 2

Design and functional validation of ECR. (A) Schematic illustrating structural design of ECR and its variants. (B) Molecular dynamics simulation of ECR structure. (C) RT-qPCR quantification of ECR expression in BMDMs treated with LNP, mRNA, or LNP-ECR (n = 3). (D) Confocal imaging of apoptotic

cardiomyocyte uptake by BMDMs expressing ECR(ΔGla), ECR(ΔMertk), full ECR, or treated with Annexin V and Mertk inhibition. DAPI (nuclei, blue), WGA (macrophage membrane, green), IVISense680-labeled apoptotic cardiomyocytes (red). Scale bars, 12.5μm. **(E)** Flow cytometric quantification of apoptotic cardiomyocyte engulfment under the indicated conditions. (F) Immunoblot analysis of γ-carboxylated Gla (c-Gla) following expression of full or variant receptors or under Annexin V or Mertk inhibition. (G) Immunoblot analysis of phosphorylated Mertk (p-Mertk) in BMDMs expressing full or variant receptors or under inhibitory treatments. (H) Rac1 activation assay in BMDMs by PAK PBD pull down of GTP Rac1. Total Rac1 were detected from input lysates. (I) RT-qPCR analysis of the expression of PI3k, AKT, ERK in BMDMs under the indicated treatment conditions (n = 3). Data are presented as mean ± SD. $^{NS}P > 0.05$, $^{*}P < 0.05$, $^{**}P < 0.01$, $^{***}P < 0.001$.

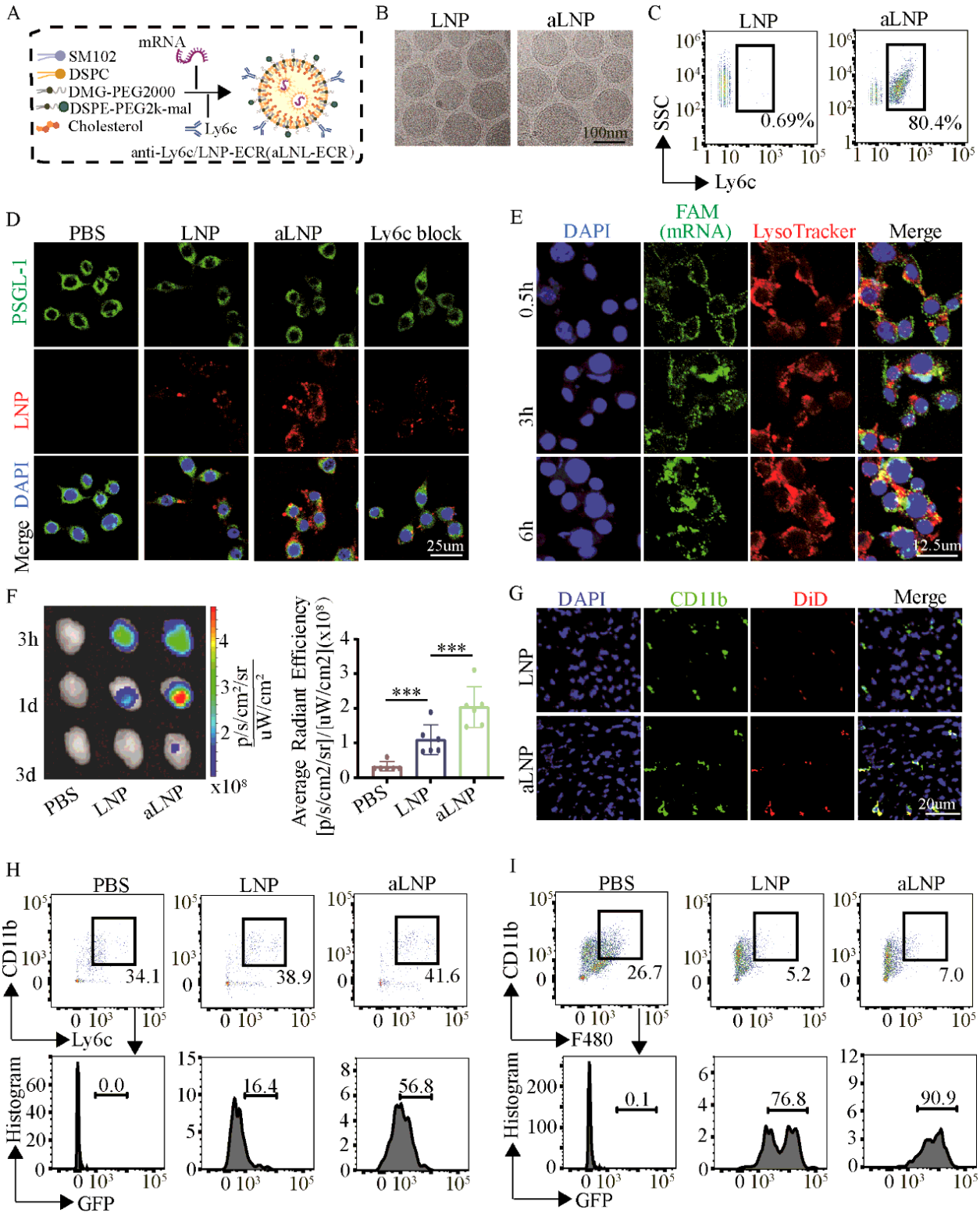


Figure 3

Design and characterization of a Ly6c-targeting LNP. (A) Schematic diagram of aLNP-ECR (aLNP) preparation. (B) Transmission electron microscopy images of LNP-ECR (LNP) and aLNP-ECR. Scale bar, 100 nm. (C) Ly6c antibody conjugation efficiency on lipid nanoparticles assessed by nano-flow cytometry. (D) Confocal imaging of BMMNCs treated with PBS, LNP-ECR, aLNP-ECR or anti-Ly6c-blocked aLNP-ECR (n = 3). DAPI (nuclei, blue), PSGL-1 (cell membrane, green), DiD-labeled LNP (red). Scale bars,

25μm. (E) Subcellular localization of aLNP-delivered mRNA in BMMNCs at indicated timepoints. DAPI (nuclei, blue), FAM-labeled mRNA (green), LysoTracker (lysosomes, red). Scale bars, 12.5μm. (F) In vivo fluorescence imaging of DiD-labeled LNP or aLNP in hearts of MI/R mice at 3, 24, and 72 h after intravenous administration, with quantitative analysis at the 3 h timepoint (n = 6). (G) Confocal images of heart sections showing colocalization of DiD-labeled LNP or aLNP with $CD11b^+$ myeloid cells in the peri-infarct region. DAPI (nuclei, blue), CD11b (green), DiD-labeled LNP (red). Scalar bar, 20μm. (H) Flow cytometric analysis of GFP expression in circulating $Ly6c^+$ monocytes 24 h after injection of PBS, ECR mRNA-loaded non-targeted LNP (LNP), or Ly6c-targeting LNP (aLNP) in MI/R mice. (I) Flow cytometric analysis of GFP expression in $F4/80^+$ macrophages isolated from infarcted cardiac tissue 24 h after intravenous administration of PBS, LNP, or aLNP. Data are presented as mean ± SD. $^{NS}P > 0.05$, $^*P < 0.05$, $^{**}P < 0.01$, $^{***}P < 0.001$.

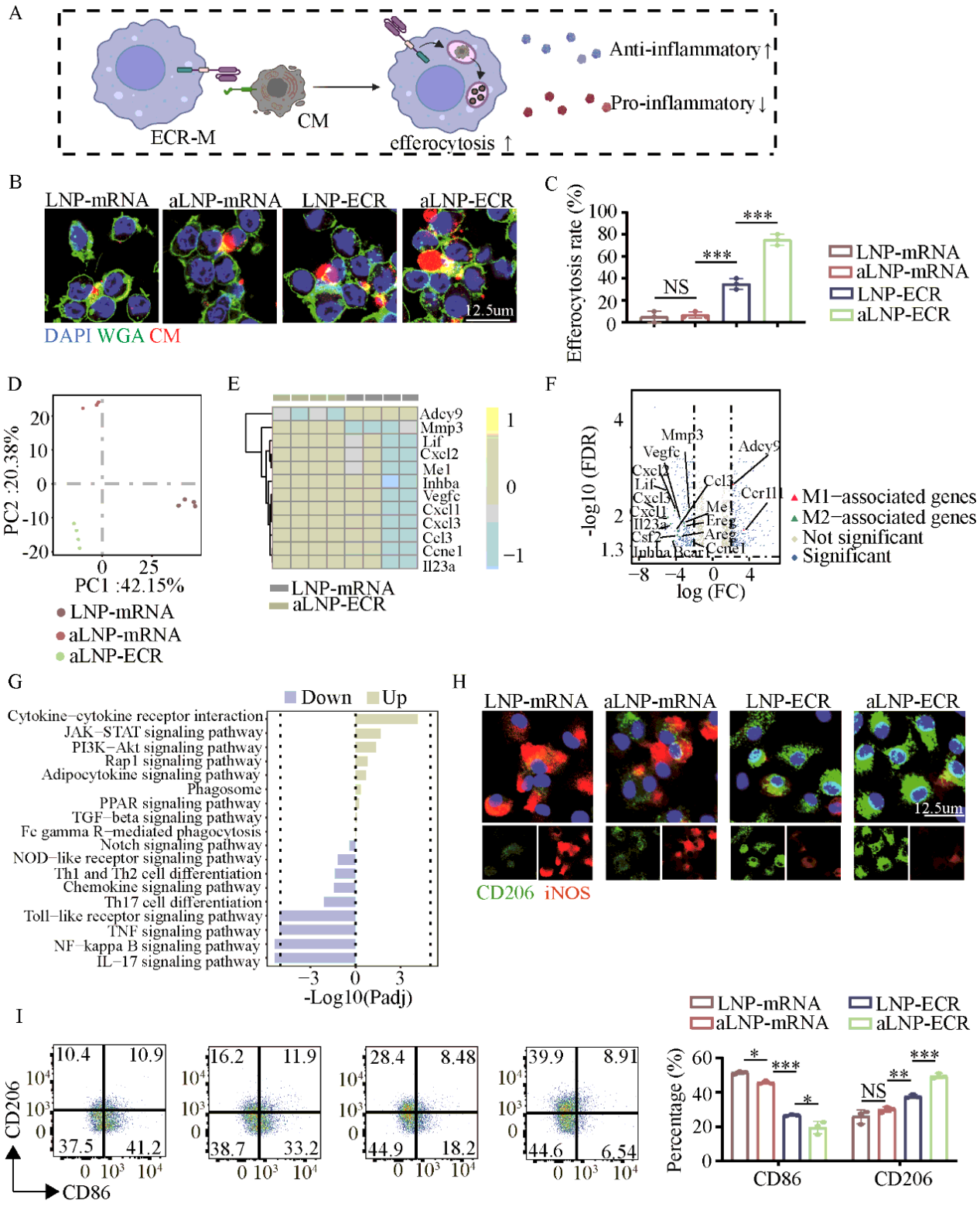


Figure 4

Functional evaluation of ECR-expressing macrophages in vitro. (A) Schematic illustrating ECR-expressing macrophages (ECR-M) engulfing apoptotic cardiomyocytes. (B) Confocal images showing the phagocytosis of apoptotic cardiomyocytes by BMDMs under LNP-mRNA, anti-Ly6c/LNP-mRNA (aLNP-mRNA), LNP-ECR or anti-Ly6c/LNP-ECR (aLNP-ECR) treatments. DAPI (nuclei, blue), WGA (macrophage membrane, green), IVISense680-labeled apoptotic cardiomyocytes (red). Scale bars, 12.5μm. **(C)**

Quantitative analysis of the phagocytosis rate of apoptotic cardiomyocytes by BMDMs treated with different treatments (n = 3)**.** (D) Principal component analysis of global gene expression profiles from LNP-mRNA, aLNP-mRNA, and aLNP-ECR treated BMDMs (n = 4). (E) Hierarchical clustering of differentially expressed genes from LNP-mRNA versus aLNP-ECR (n = 4). (F) Volcano plot of differentially expressed genes in LNP-mRNA versus aLNP-ECR. Blue indicates Padj < 0.05 and log2 fold change >1 or <−1. Red and green triangles denote significant M1- and M2-associated genes, respectively (n = 4). (G) KEGG pathway enrichment analysis of upregulated and downregulated pathways in aLNP-ECR versus LNP-mRNA. (H) Confocal images of BMDMs showing M1- and M2-associated markers after treatment with LNP-mRNA, **aLNP-mRNA, LNP-ECR, or aLNP-ECR**. DAPI (nuclei, blue), CD206 (M2, green), iNOS (M1, red). Scalar bar, 12.5 μm. (I) Flow cytometry analysis and quantification of $CD86^+$ (M1-like) and $CD206^+$ (M2-like) BMDMs under the indicated treatments (n = 3). Data are presented as mean ± SD. $^{NS}P > 0.05$, *P < 0.05, **P < 0.01, ***P < 0.001.

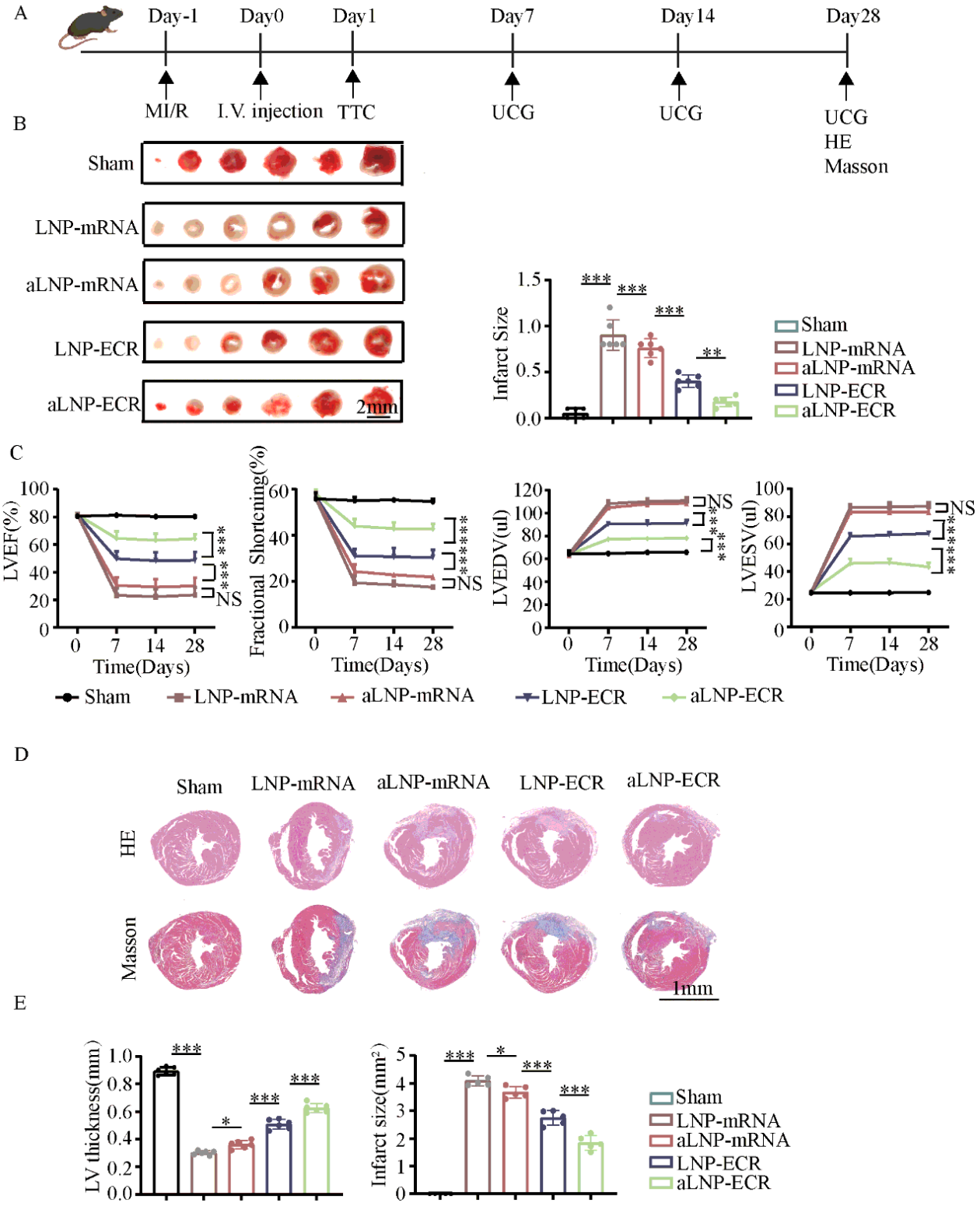


Figure 5

aLNP-ECR promotes infarct repair and functional recovery after MI/R. (A) Experimental timeline for MI/R surgery, intravenous administration, and subsequent analyses. TTC, triphenyl tetrazolium chloride; UCG, echocardiography. (B) Representative TTC-stained heart sections from sham, LNP-mRNA, aLNP-mRNA, LNP-ECR, and aLNP-ECR groups, with quantification of infarct size (n = 6). (C) Serial echocardiographic assessment of LVEF, fractional shortening, LVEDV and LVESV at baseline and indicated time points after

MI/R (n = 6). (D) Representative hematoxylin and eosin (top) and Masson's trichrome (bottom) staining of heart cross-sections harvested 28 days after MI/R. Scale bars, 1mm. (E) Quantification of left ventricular wall thickness (left) and fibrotic scar area (right) based on histological analyses in (D) (n = 6). Data are presented as mean ± SD, $^{NS}P > 0.05$, *P < 0.05, **P < 0.01, ***P < 0.001.

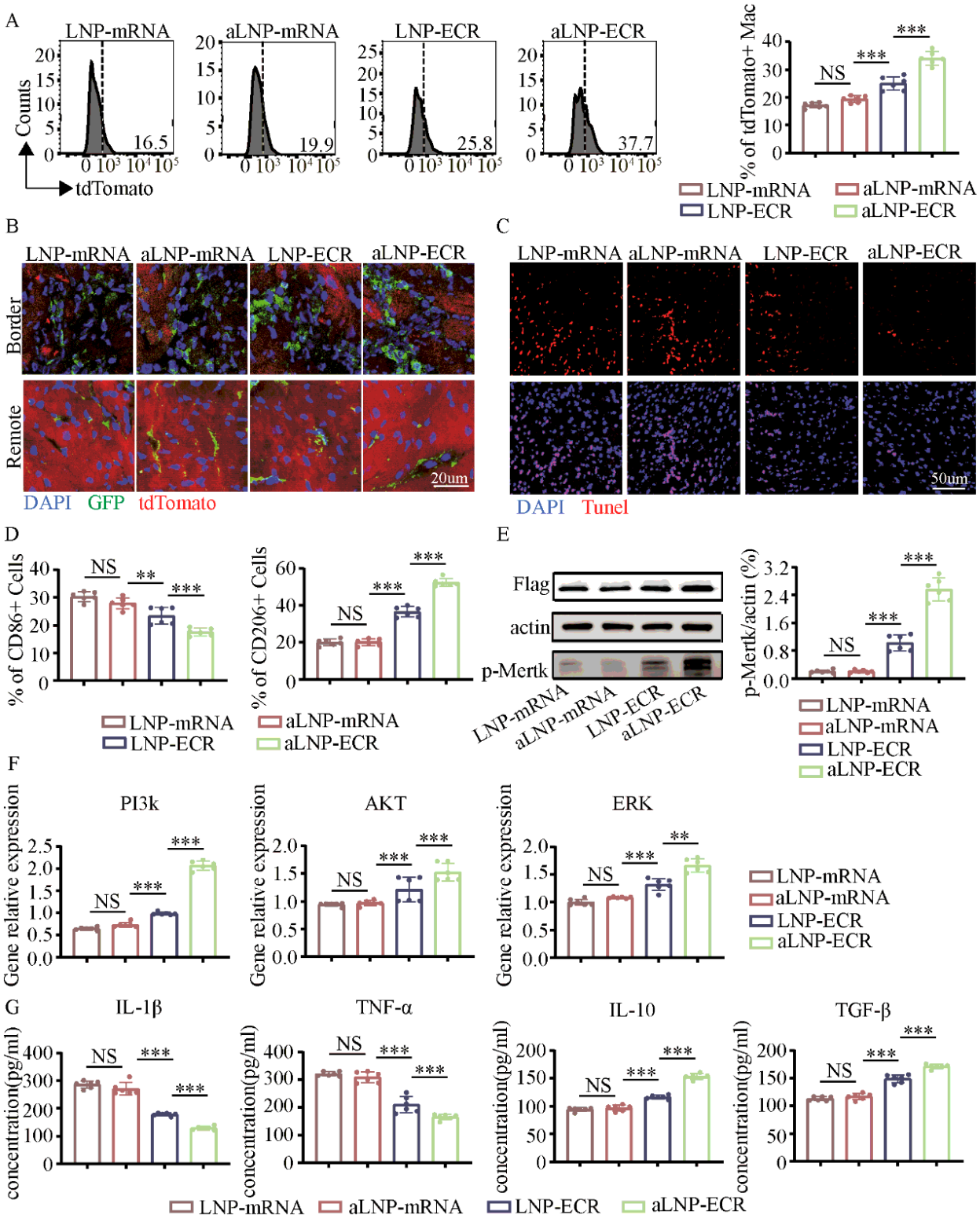


Figure 6

aLNP-ECR enhances macrophage efferocytosis and reshapes the post-infarction immune microenvironment. (A) Flow cytometric analysis and quantification of tdTomato$^+$ macrophages in hearts of MI/R mice treated with LNP-mRNA, aLNP-mRNA, LNP-ECR, or aLNP-ECR (n = 6). “tdTomato” signal indicates engulfment of cardiomyocyte-derived components by macrophages. **(B)** Confocal images showing macrophages engulfing tdTomato$^+$ cardiomyocytes in the infarct border zone (top) and remote myocardium (bottom). DAPI (nuclei, blue), GFP-ECR-M (green), tdTomato-labeled cardiomyocytes (red). Scalar bar, 20μm. (C) Tunel staining of heart sections from MI/R mice following LNP-mRNA, aLNP-mRNA, LNP-ECR or aLNP-ECR treatment. DAPI (nuclei, blue). Scale bar, 50μm. (D) Flow cytometric analysis and quantification of CD86$^+$ (M1-like) and CD206$^+$ (M2-like) macrophage subsets isolated from hearts 3 days after treatment **(n = 6). (E)** Immunoblot analysis of phosphorylation Mertk protein levels following different treatments, with quantification normalized to **β-actin (n = 6). (F)** RT-qPCR analysis of the expression of PI3k, AKT, ERK in myocardial infarct tissue after treatment with LNP-mRNA, aLNP-mRNA, LNP-ECR or aLNP-ECR (n = 6). (G) **ELISA analysis of inflammatory cytokines (IL-1β, TNF-α) and anti-inflammatory cytokines (TGF-β, IL-10) concentrations in heart homogenate of MI/R induced mice after** treatment **(n = 6).** Data are presented as mean ± SD, ^{NS}P > 0.05, *P < 0.05, **P < 0.01, ***P < 0.001.

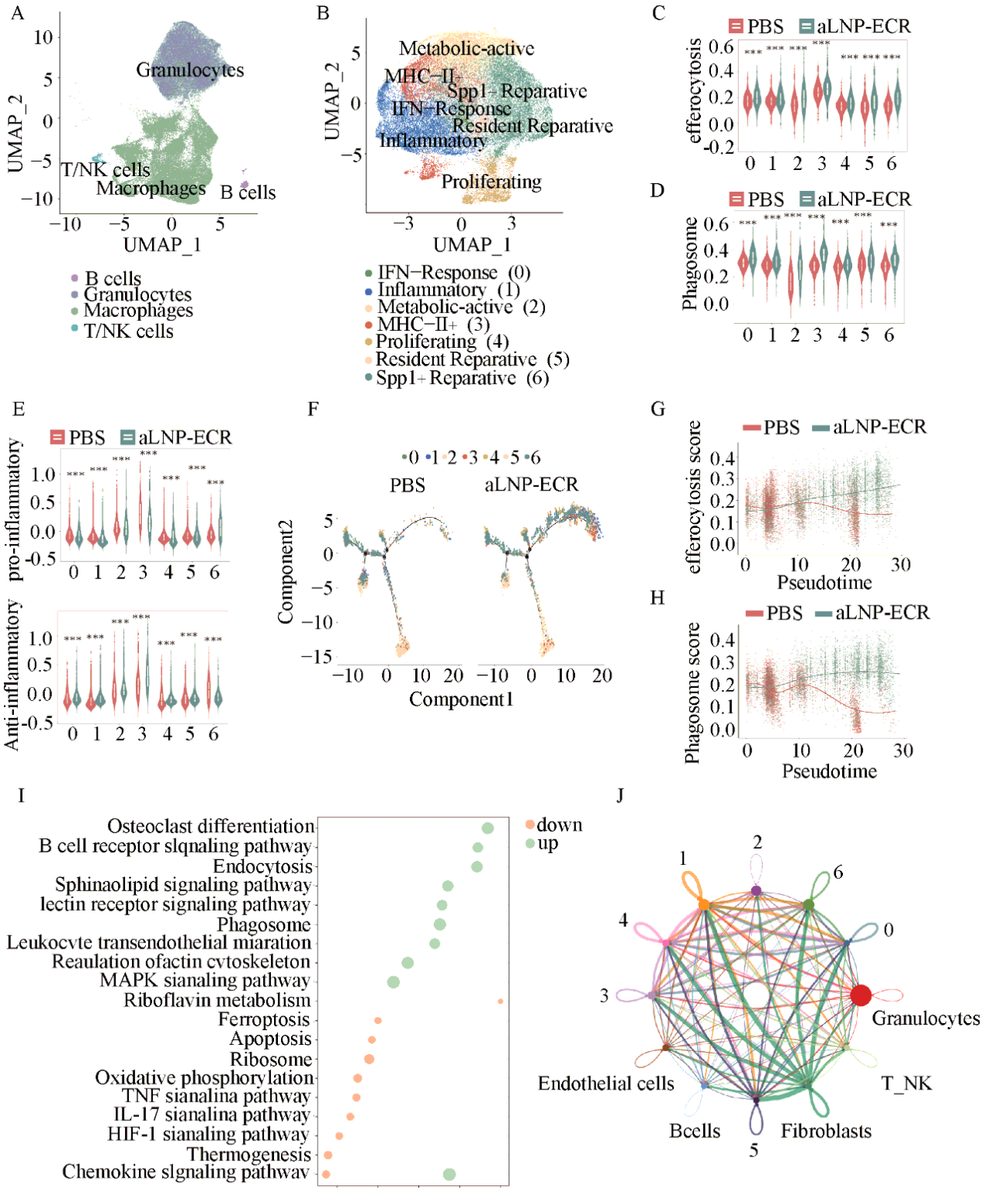


Figure 7

Single-cell transcriptomic landscape of lesional macrophages following aLNP-ECR treatment. (A) UMAP of leukocytes isolated from infarct regions of MI/R hearts treated with PBS or aLNP-ECR, identifying four major immune cell populations based on canonical marker gene expression. Cell types are color-coded and include macrophages, granulocytes, B cells, and T/NK cells. (B) UMAP visualization of reclustered cardiac macrophages from infarct regions, identifying seven transcriptionally distinct macrophage

states, including inflammatory, Interferon (IFN)-responsive, metabolic-active, MHC-II$^+$ Antigen-presenting, proliferating, resident reparative and Spp1+ reparative subsets. (C) Efferocytic score across the seven macrophage subsets in PBS and aLNP-ECR groups (n = 3). (D) Phagosome-lysosome gene signature scores across macrophage subsets in PBS and aLNP-ECR groups (n = 3). (E) Pro-inflammatory gene (top) and anti-inflammatory gene (bottom) signature scores across macrophage subsets in PBS and aLNP-ECR groups (n = 3). (F) Pseudotime analysis of lesional macrophages following PBS or aLNP-ECR treatment. Cells from PBS treated and aLNP-ECR treated hearts are projected onto the inferred macrophage trajectory, colored by macrophage subset identity. Differences in macrophage distribution along pseudotime are observed between treatment groups. (G) Efferocytosis-related gene signature scores along the macrophage pseudotime trajectory in PBS treated (red) and aLNP-ECR treated (green) hearts. Smoothed module scores are plotted as a function of pseudotime (n = 3). (H) Phagosome-lysosome gene signature scores along the macrophage pseudotime trajectory in PBS treated (red) and aLNP-ECR treated (green) hearts. Smoothed module scores are plotted as a function of pseudotime (n = 3). (I) Dot plot showing pathway enrichment analysis of differentially expressed genes in lesional macrophages following aLNP-ECR treatment. Dot size indicates the degree of pathway enrichment, and color denotes upregulated or downregulated pathways. (J) Cell-cell communication network inferred from ligand-receptor interactions between macrophage subsets and major cardiac cell types, including fibroblasts, endothelial cells, granulocytes, and lymphocytes. Data are presented as mean ± SD, ***P < 0.001.

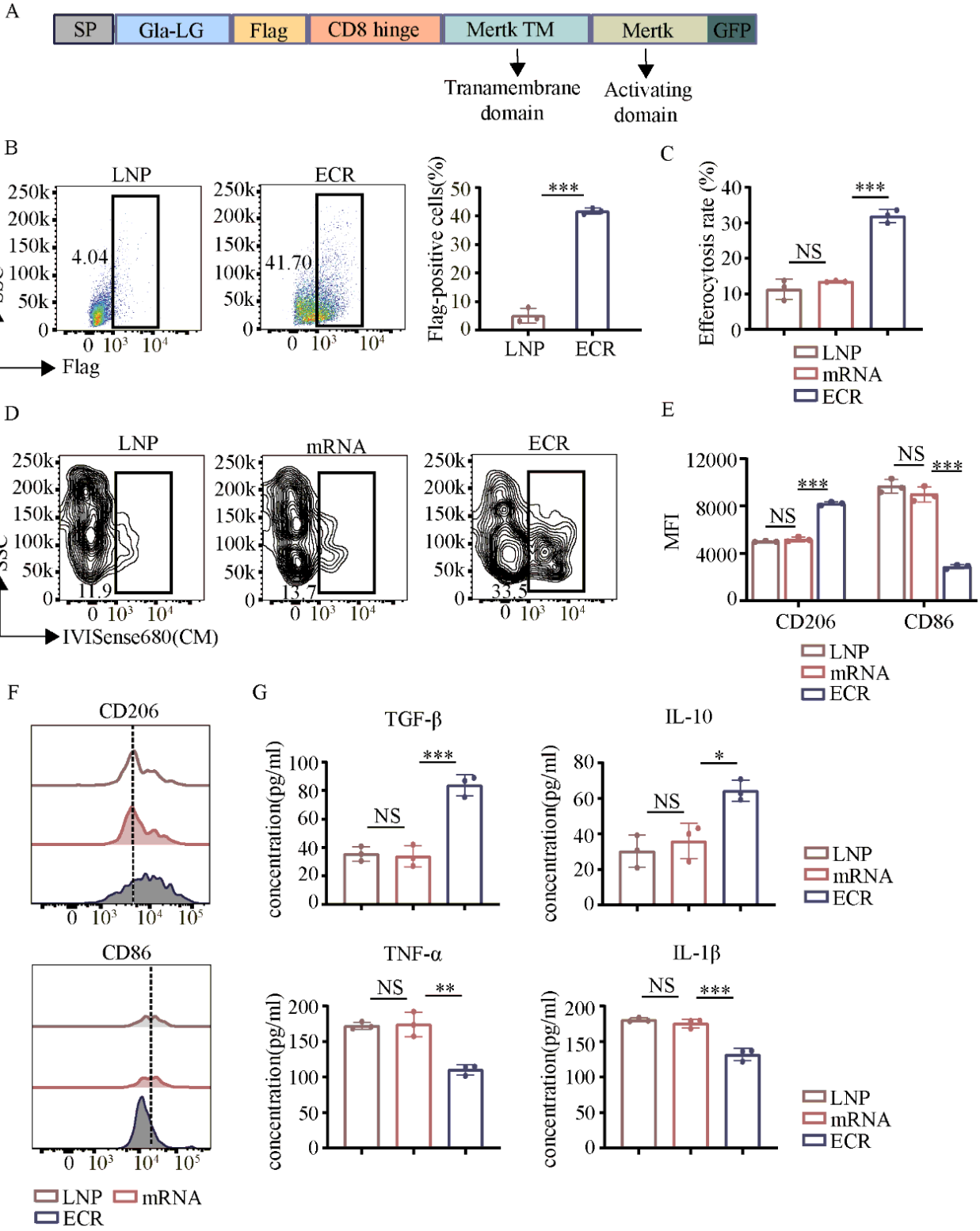


Figure 8

Generation and characterization of human ECR. (A) Schematic representation of the human ECR construct, comprising a Gas6-derived Gla-LG extracellular module for PS recognition, a human CD8α hinge, and the transmembrane and intracellular signaling domains of human Mertk, together with a Flag tag and GFP reporter. (B) Representative flow cytometric analysis and quantification of Flag-positive human macrophages 24 h after LNP-mediated mRNA delivery (n = 3). (C–D) Flow cytometric analysis (C)

and quantification (D) of efferocytosis of fluorescently labeled apoptotic cardiomyocytes by human macrophages subjected to the indicated treatments (n = 3). (E–F) Representative flow cytometric profiles (F) and quantitative analysis (E) of M2-associated (CD206) and M1-associated (CD86) marker expression in human macrophages following indicated treatments. (G) ELISA-based quantification of anti-inflammatory cytokines (TGF-β, IL-10) and pro-inflammatory cytokines (TNF-α, IL-1β) in supernatants from human macrophages following indicated treatments (n = 3). **Data are presented as mean ± SD, ^{NS}P > 0.05, *P < 0.05, *P < 0.01, *P < 0.001.**

Supplementary Files

This is a list of supplementary files associated with this preprint. Click to download.

- SupportingInformation.docx